

# Current-readout technique for ultra-high-rate experiments

Maki Wakata,<sup>1</sup> Shoei Akamatsu,<sup>1</sup> Takuhiro Fujii,<sup>1</sup> Taisei Furuyama,<sup>1</sup> Lisa Hara,<sup>1</sup> Yumi Ishikawa,<sup>1</sup> Tadashi Ito,<sup>1</sup> Takahiro Kikuchi,<sup>1</sup> Tsutomu Mibe,<sup>2</sup> Sachi Ozaki,<sup>1</sup> Mitsuhiko Yokomizo,<sup>1</sup> and Jiro Murata<sup>1,\*</sup>

<sup>1</sup>*Department of Physics, Rikkyo University, Tokyo 171-8501, Japan*

<sup>2</sup>*Institute of Particle and Nuclear Studies (IPNS), 1-1 Oho, Tsukuba, Ibaraki 305-0801 Japan*

(Dated: June 26, 2024)

This study developed a new current-readout technique capable of handling measurements with high count rates reaching 1 Gcps. By directly capturing the output current of a photomultiplier as a digitized waveform, we estimated event rates, overcoming the limitations imposed by pulse pileup constraints and deadtimes. This innovative method was applied to a muon spin rotation/relaxation/resonance experiment at the Japan Proton Accelerator Research Complex, demonstrating its anticipated performance. Furthermore, we explored methods for estimating statistical uncertainty and investigated potential applications in analog-logic OR/AND gates. Our findings reveal that the developed technique opens avenues for developing future non-binary logic circuits operating based on  $n$ -adic numbers.

## I. INTRODUCTION

Handling high-rate counting scenarios with rates of over mega counts per second (Mcps) is a crucial technical requirement for conducting experiments at high-intensity accelerator facilities. For instance, a muon beam at the Materials and Life Science Experimental Facility of the Japan Proton Accelerator Research Complex (J-PARC MLF) is expected to have an intensity of  $N_\mu = 10^5 \sim 10^6$  ppp (particles/beam-pulse) [1]. It means that the muon decay rate is expected to be  $N_\mu/\tau_\mu \sim 100$  Gcps, considering the muon's lifetime of  $\tau_\mu = 2.2 \mu\text{s}$ . To exploit such high-intensity beams, a detector may be required to handle a counting rate of 1 Gcps per channel if it covers a solid angle of  $\sim 1\%$  of  $4\pi$ . However, considering that the time scale of a typical detector is  $\sim 10$  ns, counting pulses at over  $1/(10 \text{ ns}) \rightarrow 100$  Mcps becomes impossible owing to signal pulse pileups. Consequently, fine segmentation aimed at reducing the solid angle of each detector channel and ultra-fast devices aimed at shortening the time scales are usually adopted. In simple radiation-rate-measuring experiments not requiring event-by-event assessments, identifying individual pulse signals from detectors is unnecessary. Relevant examples of such experiments include simple lifetime and muon spin rotation/relaxation/resonance ( $\mu\text{SR}$ ) measurements with negligible backgrounds. In this case, the only required information is the positron/electron flux,  $n_e(t)$  (with  $t = 0$  denoting the beam-pulse-arrival timing), hitting the detector. In this study, we employed digitizer readouts to record the output currents of photomultiplier tubes (PMTs), thus testing their ability to handle a hitting rate of  $n_e \sim 100$  Mcps. Notably, numbers of similar waveform digitizing approaches have been adopted [2–6]. While most of these studies aimed to reject pileup events by offline analysis, this study, on the contrary, actively records pileup events to enable

high-rate measurements. After developing a system for this current-readout method, we demonstrated the effective application of the developed technique to muon-lifetime and  $\mu\text{SR}$  measurements at the J-PARC. Furthermore, we also discovered a new technique for accomplishing coincidence measurements between multiple detector channels for background event suppression. Remarkably, the application scope of this technique extends beyond radiation-detection applications to general binary logic circuits, enhancing their information density by utilizing non-binary,  $n$ -decimal numbers.

## II. EXPERIMENT

We are preparing to execute a new experiment, labeled as the muon Lorentz violation ( $\mu\text{LV}$ ) experiment, to perform high-precision muon-lifetime and  $\mu\text{SR}$  measurements utilizing the pulsed muon beam produced at the J-PARC MLF [7, 8]. The scientific aim is to compare the shapes of decay spectra,  $n_e(t)$ , obtained under varying conditions, without requiring absolute precision in lifetime and spin-precession parameters (such as the Larmor frequency,  $\omega_L$ ). The demonstration experiment involved in this study has been designed to count the number of positrons resulting from  $\mu^+ \rightarrow e^+ + \bar{\nu}_\mu + \nu_e$  decays that hit single plastic scintillation counters at a counting rate exceeding 100 Mcps, without establishing coincidence pairs. Fig.1 presents the experimental setup for the tests, labeled as  $\mu\text{LV}$ -Run0 and Run1, comprising three plastic scintillation counters with PMT readouts. In addition to these, the setup has other plastic scintillation counters finely segmented into 1,280 channels (forming double layers to generate 640 coincidence pairs) with multi-pixel photon counter readouts, known as Kalliope detector [9]. This Kalliope is a common-use facility permanently set at the beamline, adopted as a reference in this study for comparisons with our system. The primary objective of this study is to overcome the known counting-rate saturation of Kalliope at  $\sim 1$  Mcps,

---

\* corresponding author: jiro@rikkyo.ac.jp

attributed to pulse-processing deadtimes and signal pile-ups.

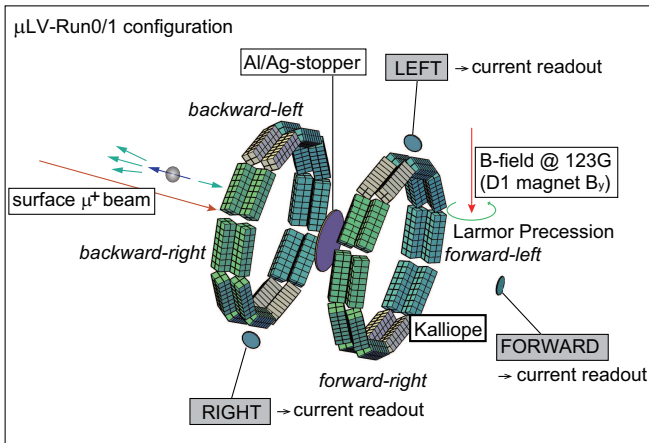


FIG. 1. Experimental setup of the  $\mu$ LV-Run0 and Run1 experiments. The framework includes three plastic scintillation counters (LEFT, RIGHT, and FORWARD), along with the Kalliope detector, comprising a 640-ch-inner-plastic-layer and 640-ch-outer-layer [9].

PMTs with thin plastic scintillators were employed to detect positrons emitted from the decay of positive surface muons stopped within an aluminum sheet with a diameter of 10 cm and thickness of 2 mm (for Run0) or a silver sheet with a thickness of 1mm (for Run1). Specifically, a 3 GeV proton beam was directed at a graphite target to produce pions, which then decayed into muons that stopped at the surface of the production target, creating a “surface muon beam” with an energy of 4.1 MeV. This muon beam featured a double-pulse structure comprising two 100-ns-wide pulses separated by a 600-ns-interval, along with a beam repetition rate of  $f_{\text{cycle}} = 1/T_{\text{cycle}} = 25$  Hz [10].

The typical time-averaged intensity of the surface muon beam could reach as high as  $I_{\text{beam}}^{\text{max}} = 10^7$  muons per second ( $\mu/s$ ), with the 3 GeV synchrotron operating at a power of 700 kW. This beam intensity corresponds to a muon intensity of  $N_{\mu} = I_{\text{beam}}^{\text{max}}/(25 \text{ double-pulses/s}) = 4 \times 10^5$  ppp. The maximum decay rate can be estimated as follows:

$$n_{\text{decay}}(t) = -\frac{dN_{\mu}}{dt} = \frac{N_{\mu}}{\tau_{\mu}} e^{-t/\tau_{\mu}} \sim 2 \times 10^{11} /s \quad (\text{at } t = 0). \quad (1)$$

The solid angle covered by a pair of  $10 \times 10 \times 12$  mm plastic scintillators within the Kalliope setup is  $\Omega_{\text{Kalliope}} = 3.6 \times 10^{-4}$ . Thus, the expected event rate for one Kalliope channel is  $n_{\text{decay}}(t) \times \Omega_{\text{Kalliope}} \sim 70$  Mcps, which exceeds the handling capacity of the electronic equipment within Kalliope. To address this, collimators and slits are usually positioned at the beamline to reduce the beam intensity to  $1/10 \sim 1/100$  of  $I_{\text{beam}}^{\text{max}}$ . However, even higher

beam intensities of  $I_{\text{beam}} \sim 10^8 \mu/s$  are anticipated at other new beamlines within the MLF, H-line, for example [11]. This study aims to overcome this bottleneck, thus being able to utilize the maximum beam intensity produced at the J-PARC.

In this study, measurements were performed using beams with intensities of  $I_{\text{beam}}^{\text{FULL}} = 4.8 \times 10^6 \mu/s$  (“FULL-intensity” beam) and  $I_{\text{beam}}^{\text{NORMAL}} = 7.4 \times 10^5 \mu/s$  (“NORMAL-intensity” beam), obtained by tuning the beamline slits and a lead beam-collimator under  $\sim 730$  kW power operation of the 3 GeV proton synchrotron. Refer to Appendix A for details on the beam intensity estimation.

The NORMAL-intensity beam is recommended for users performing  $\mu$ SR experiments at the D1 area to avoid detector saturation effects. For our experiments, three PMTs (with a photocathode featuring a diameter of 25 mm, Hamamatsu H7415 [12]) with thin plastic scintillators (30 mm diameter, BC408, denoted as LEFT, RIGHT, and FORWARD in Fig.1) were employed. The two sideward plastic scintillators (LEFT and RIGHT, with a thickness of 1 mm) were placed with their centers located at a horizontal distance of 360 mm and a vertical downward distance of 76 mm from the center of the stopper (beamline height). Considering that the solid angle of these LEFT or RIGHT counters was  $\Omega_{\text{PMT}} = 4.2 \times 10^{-4}$ , their maximum expected counting rate for  $I_{\text{beam}}^{\text{FULL}}$  was

$$n_{\text{LEFT}} = n_{\text{RIGHT}} = n_{\text{decay}} \Omega_{\text{PMT}} \sim 20 \text{ Mcps } (t = 0). \quad (2)$$

The FORWARD counter (with a thickness of 0.5 mm) was set at a position located 360 mm downstream and 76 mm below the beamline to monitor downstream radiation.

The scintillator planes of the LEFT and RIGHT counters were set parallel to the beam direction to suppress the detection of upstream radiation. Conversely, the FORWARD counter was positioned along the upstream direction to detect positrons from the stopper, along with other types of radiation traveling along the upstream direction. This upstream radiation, more intense than the collimated beam flux by an order of magnitude, is typically undesired in scientific measurements but was utilized in this study for high-intensity tests.

Fig.2 illustrates the typical output voltage signal recorded by an oscilloscope with an input termination resistance of  $R_T = 50 \Omega$ . Here, the pulse width (full width at half maximum) was  $\sim 6$  ns, indicating the occurrence of pileup at periodic counting rates of over  $\sim 200$  MHz. Notably, conventional pulse-counting techniques using voltage discriminators cannot handle  $I_{\text{beam}}^{\text{max}}$  owing to pileup issues. In practical situations, the data-handling deadtime emerges as a bottleneck before the pileup frequency of the detector is reached. For instance, Kalliope features a deadtime of  $\sim 100$  ns, owing to which counting losses begin at  $\sim 1/100 \text{ ns} = 10$  MHz. For random arrival times, significant counting losses begin at lower frequencies, that is, at a counting rate of  $\sim 1$  Mcps. The Kalliope system indeed experiences such a counting

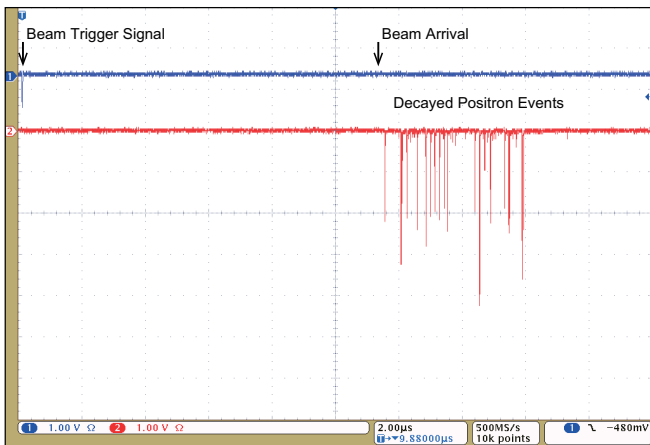


FIG. 2. Typical voltage profile of the LEFT counter at  $\sim 5$  Mcps with FULL-intensity beam, recorded by an oscilloscope.

loss at a typical beam intensity of  $10^5 \mu/s \sim I_{\text{beam}}^{\text{NORMAL}}$ , prompting users to set this as the maximum beam intensity.

To overcome this counting-rate bottleneck, we developed a current-readout technique for lifetime and  $\mu\text{SR}$  experiments. This technique is immune to pileup and deadtime effects. The only remaining bottlenecks include the intrinsic saturation of the PMTs and the maximum acceptable voltage of the readout device.

For this purpose, we adopted a flash analog-to-digital converter (FADC) waveform digitizer (CAEN DT5370SB [13]) to record the output voltage waveforms of the PMTs, whose inputs were terminated using resistors with a resistance of  $R_T = 50 \Omega$ . The adopted digitizer features a sampling rate of  $f_s = 500$  MHz, along with a 14-bit voltage resolution and eight input channels. Recorded data stored within the buffer memory (5.12 M samples/channel) of the digitizer can be transferred to computers via a USB/optical link.

Considering the data transfer speeds of Optical-Link (80 Mbps) and USB 2.0 (30 Mbps), we set the data-acceptance time window to  $T_w = 150 \mu\text{s}$ , synchronizing it with the data recording trigger signal instant ( $t = 0$ ). The trigger signals were generated based on the beam pulse timing at  $f_{\text{cycle}}$ , provided by the 3 GeV synchrotron control signal. The value of  $T_w$  was chosen to adequately observe the desired scientific phenomena and to allow data transfer to a storage device at the required data transfer speed.

### III. PRINCIPLE

#### A. Electric Circuits

If we are interested in investigating relatively slow phenomena with a timescale on the order of  $\mu\text{s}$ , as in the current study, a time resolution of  $\sigma_t \sim 100$  ns, for instance,

is sufficient to observe the time spectra of  $n_e(t)$ . In such cases, identifying discrete pulse signals with ns precision, as required in conventional event-by-event pulse counting, is unnecessary. Instead, obtaining their averaged flux (event rate) information (i.e., current) as a function of time  $t$  with a resolution of  $\sigma_t$  is adequate. Therefore, in this study, we attempted to obtain flux information from the output electric currents  $i(t)$  of the PMTs.

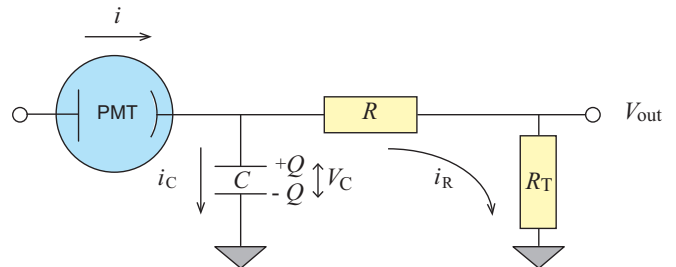


FIG. 3. Equivalent electric circuit for PMT readout. Here, the PMT acts as a current source, and  $V_{\text{out}}$  denotes the voltage to be measured.

Fig.3 shows the equivalent electric circuit for the expected voltage,  $V_{\text{out}}$ , considering that a PMT is a current source [14]. The termination resistance,  $R_T$ , satisfies the following differential equation:

$$i(t) = C \frac{R + R_T}{R_T} \frac{dV_{\text{out}}(t)}{dt} + \frac{V_{\text{out}}(t)}{R_T}. \quad (3)$$

The above relation is derived based on the following:

$$\begin{aligned} i &= i_C + i_R, \\ i_C &= \frac{dQ}{dt} = C \frac{dV_C}{dt}, \\ V_C &= V_{\text{out}} + i_R R, \\ V_{\text{out}} &= i_R R_T, \end{aligned} \quad (4)$$

where  $C$  denotes the total capacitance of the PMT and the signal cable, with a typical value of  $\sim 100$  pF. Given that the series resistance,  $R$ , of the cable must be extremely small, we can assume that  $R/R_T \ll 1$  in usual cases. Thus, Eq.(3) simplifies to

$$i(t) \sim C \frac{dV_{\text{out}}(t)}{dt} + \frac{V_{\text{out}}(t)}{R_T}. \quad (5)$$

The characteristics of the solution of Eq.(5) are well known, as described in Knoll's textbook [14]. If the input current  $i(t)$  exhibits a narrow pulse structure, the solution,  $V_{\text{out}}(t)$ , is anticipated to display a pulse shape with a rising time corresponding to the width of the input current. A time constant  $\tau_c = R_T C$  represents the exponential falling time. Accordingly,  $V_{\text{out}}(t)$ , read between the digitizer's input resistor  $R_T$ , represents the output current  $i(t)$ , whose averaged value is proportional to the number of photons produced within the scintillator.

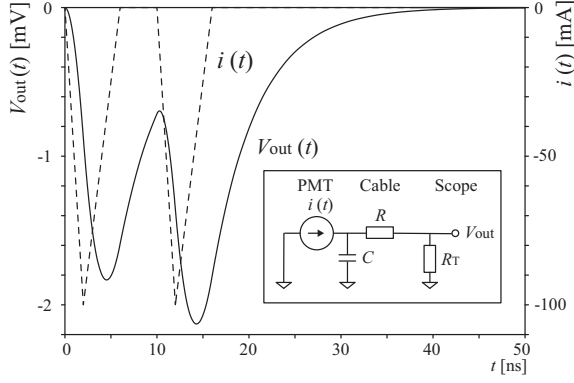


FIG. 4. Results of the circuit simulation conducted using LTspice, assuming parameter values of  $C = 10$  pF,  $R_T = 50 \Omega$ , and  $R = 0.1 \Omega$  and assuming that  $i(t)$  generates  $V_{\text{out}}(t)$  [15].

This estimation was confirmed by performing a circuit simulation (LTspice [15]), and the results of this simulation are shown in Fig.4. In this simulation, the input signal comprised a pair of closely spaced triangular current pulses, as illustrated in the figure. As anticipated, the output voltage signals,  $V_{\text{out}}(t)$ , were nearly proportional to the input current,  $i(t)$ , with a decay time constant of  $\tau_c$ . This result demonstrates the pileup phenomenon between two output voltage pulses. To overcome this bottleneck, we must acknowledge that such pileup data contains two independent events.

The quantity to be measured is the number of positrons hitting the detector, rather than the number of photons generated by scintillators. The number of photons corresponding to a single positron penetration event typically fluctuates owing to the changing path lengths of positrons penetrating the scintillators, statistical variations in the number of photons, and statistical fluctuations in the number of secondary electrons generated within the PMTs. These complex pulse-to-pulse charge fluctuations can be avoided through discrimination when applying the conventional pulse-counting method. On the other hand, these analog fluctuations are anticipated to influence the final precision of the flux measurement in the present method. Therefore, the final precision for  $n_e(t)$  may be worse than that in the conventional pulse-counting method; consequently, we must quantitatively estimate the contributions of these additional fluctuations, as discussed in Section III C.

## B. Statistics

Let us first consider counting statistics. In the conventional pulse-counting method, the measured event number,  $\tilde{N}$ , is generally considered the best estimate of the expected event number,  $N$ , for the detector. In this estimation, for sufficiently large  $\tilde{N}$ , where a Poisson distri-

bution approximating a symmetric Gaussian distribution can be assumed, the statistical uncertainty of  $\tilde{N}$  can be estimated as follows:

$$\sigma_{\tilde{N}} = \sqrt{\tilde{N}} \rightarrow \sim \sqrt{\tilde{N}}, \quad (6)$$

Conversely, if the statistics are low, confidence intervals for the Poisson distribution are required, resulting in asymmetric statistical error bars. This is the standard approach for estimating statistical uncertainties in the conventional pulse-counting method.

### double beam-pulse

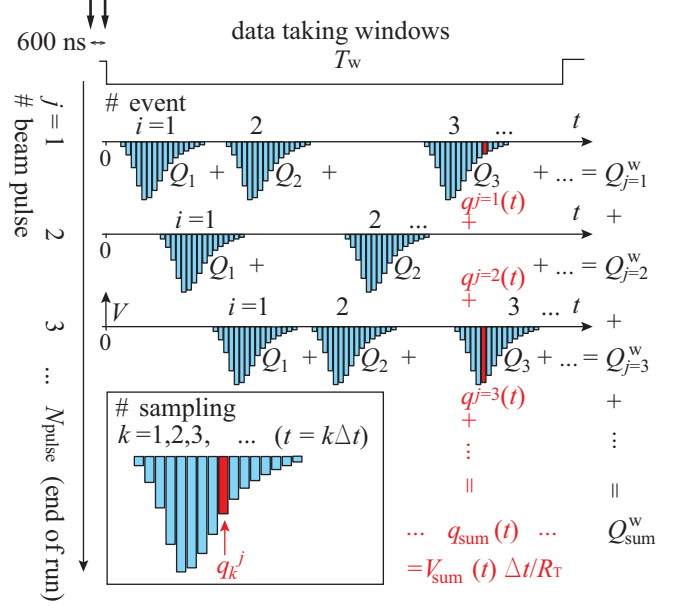


FIG. 5. Definitions of terms denoting the recorded time sequence data.  $j$  denotes the beam pulse number, ranging from  $j = 1, 2, \dots, N_{\text{pulse}}$  over a data-collection run (typically lasting 1 h).  $T_w$  represents the fixed recording time window starting after every beam pulse triggering signal.  $i$  denotes the event number during  $T_w$  beginning after each beam pulse.  $Q_i$  is the total charge flowing through  $R_T$  during the  $i$ -th event pulse.  $Q_j^w = Q_1 + Q_2 + \dots$  represents the sum of charges flowing during the  $j$ -th beam pulse.  $Q_{\text{sum}}^w = \sum_j^{N_{\text{pulse}}} Q_j^w$  denotes the total sum obtained in the data-collection run. For every  $j$ -th beam pulse, initial time sequence data are denoted as  $q^j(t)$ , where  $t = k\Delta t$ . Here,  $k$  is the sample's time-bin number and the sampling time step is  $\Delta t = 2$  ns.  $t = 0$  is defined as the beam pulse arriving timing for each  $j$ .  $q_{\text{sum}}(t) = \sum_j^{N_{\text{pulse}}} q^j(t)$  represents the beam pulse integrated time sequence data.

For analog measurements, as those in the present study, the summed charge of  $N$  events is expressed as follows:

$$Q_{\text{sum}} = Q_1 + Q_2 + Q_3 + \dots + Q_N, \quad (7)$$

where  $Q_i$  ( $Q_i > 0$ ) represents the charge output from the  $i$ -th hit on the detector.  $Q_i$  can be derived from the time integration of the current waveform over the pulse region, as illustrated in Fig.5.

In addition to the statistical fluctuation in  $N$ , represented by the Poisson error  $\sqrt{N}$ , we must also compute the charge fluctuation,  $\sigma_Q$ , around the averaged charge,  $Q_0$ , for a single hit event using the relative uncertainty  $\hat{\sigma}_Q$ , as follows:

$$Q_0 \pm \sigma_Q = Q_0 \left( 1 \pm \frac{\sigma_Q}{Q_0} \right) = Q_0 (1 \pm \hat{\sigma}_Q). \quad (8)$$

The expected value of  $Q_{\text{sum}}$  and its uncertainty  $\sigma_{Q_{\text{sum}}}^{\text{fluctuation}}$  can then be estimated as

$$Q_{\text{sum}} = N \times Q_0 \rightarrow \sim \tilde{N} \times Q_0, \quad (9)$$

and

$$\begin{aligned} \sigma_{Q_{\text{sum}}}^{\text{fluctuation}} &= \sqrt{\sigma_Q^2 + \sigma_Q^2 + \dots + \sigma_Q^2} = \sqrt{N \times \sigma_Q^2} \\ &= \sqrt{N} \times \sigma_Q \rightarrow \sim \sqrt{\tilde{N}} \times \sigma_Q, \end{aligned} \quad (10)$$

where the event number,  $N$ , is replaced with  $\tilde{N}$ , similar to that in Eq.(6). Thus, Poisson statistics yield the following statistical fluctuation:

$$\sigma_{Q_{\text{sum}}}^{\text{stat.}} = \sigma_{\tilde{N}} \times Q_0 = \sqrt{\tilde{N}} \times Q_0. \quad (11)$$

Utilizing Eq.(9), we can estimate  $\tilde{N}$  from the measured value of  $Q_{\text{sum}}$  if  $Q_0$  is known:

$$\tilde{N} = \frac{Q_{\text{sum}}}{Q_0}. \quad (12)$$

Considering the convolution of the uncertainty sources expressed in Eqs.(10) and (11), the combined fluctuation  $\sigma_{Q_{\text{sum}}}$  can be estimated as follows:

$$\begin{aligned} \sigma_{Q_{\text{sum}}} &= \sqrt{(\sigma_{Q_{\text{sum}}}^{\text{stat.}})^2 + (\sigma_{Q_{\text{sum}}}^{\text{fluctuation}})^2} \\ &= \sqrt{\tilde{N}Q_0^2 + \tilde{N}\sigma_Q^2} \\ &= \sqrt{\tilde{N}Q_0} \sqrt{1 + \left(\frac{\sigma_Q}{Q_0}\right)^2} \\ &= \sigma_{Q_{\text{sum}}}^{\text{stat.}} \sqrt{1 + \hat{\sigma}_Q^2}. \end{aligned} \quad (13)$$

Based on this, we have

$$\sigma_{Q_{\text{sum}}} = a \times \sigma_{Q_{\text{sum}}}^{\text{stat.}} \quad (a = \text{const.}). \quad (14)$$

To derive Eq.(13), using Eq.(9) to propagate uncertainty on  $\tilde{N}$  and  $Q_0$  may seem more straightforward:

$$\sigma_{Q_{\text{sum}}}^2 = \left(\frac{\partial Q_{\text{sum}}}{\partial \tilde{N}}\right)^2 \sigma_{\tilde{N}}^2 + \left(\frac{\partial Q_{\text{sum}}}{\partial Q_0}\right)^2 \sigma_{Q_0}^2; \quad (15)$$

however, this approach is incorrect because the actual charge,  $Q_i$ , in Eq.(7) is not constant but fluctuates around  $Q_0$ .

Thus, in Eq.(13), the additional fluctuation beyond the Poisson error is regarded as a constant modification factor  $a = \sqrt{1 + \hat{\sigma}_Q^2}$ . If this additional fluctuation is considered as an offset, for instance,  $\sigma_{Q_{\text{sum}}} = \sigma_{Q_{\text{sum}}}^{\text{stat.}} + \text{const.}$ , it must dominate the total precision for high statistical data with large  $\tilde{N}$ . Eq.(14) shows that we can improve the total precision by increasing the statistics, similar to that in the conventional pulse-counting method.

### C. Voltage Fluctuation

Let us consider a charge value measured during the single time bin of the digitizer (sampling time step  $\Delta t$ ). The charge,  $q$ , included within the  $k$ -th time bin, as shown in the inset of Fig.5, is obtained from the current,  $i$ , flowing through the termination resistor,  $R_T$ , and the readout voltage  $V_{\text{out}}(t)$  as follows:

$$q(t) = i(t) \Delta t = -\frac{V_{\text{out}}(t)}{R_T} \Delta t, \quad (16)$$

where  $t = k\Delta t$  is the  $k$ -th sampling timing. The sampling frequency of the digitizer results in a sampling time step of  $\Delta t = 1/f_s$ . Importantly, for products based on the flash ADC technique,  $V_{\text{out}}$  is not obtained through charge integration during  $\Delta t$  (i.e.,  $q(t)$ ) but is determined by simply noting the voltage at the sampling timing. Consequently,  $Q$  and  $q$  are noisier compared to those obtained by conventional charge-to-digital converters (QDCs).

In the context of lifetime or  $\mu\text{SR}$  measurements, time-to-digital converter (TDC) spectra are of particular interest. Instead of plotting the counting number on the vertical axis of the TDC histogram (time spectra), we plot the ‘‘beam-pulse-integrated voltage,  $V_{\text{sum}}$ ’’ in this study because the output voltage is nearly proportional to the event rate, as indicated in Eq.(5).

The output voltage  $V^j(t)$  is recorded for every  $j$ -th beam pulse, where  $t$  is defined as the local time beginning at the beam triggering instant of each beam pulse, as shown in Fig.5. This is similar to the phenomenon shown in Fig.2 for a single beam pulse. Subsequently, individual voltages are summed over various  $j$ -th beam pulses ( $j = 1, 2, \dots, N_{\text{pulse}}$ ) within a data-collection run (e.g., for  $T_{\text{run}} = N_{\text{pulse}}/N_{\text{cycle}} \sim 1$  h), yielding

$$\begin{aligned} V_{\text{sum}}(t) &= -\sum_j^{\text{run}} V^j(t) \\ &= \sum_j q^j(t) R_T / \Delta t \\ &= q_{\text{sum}}(t) R_T / \Delta t, \end{aligned} \quad (17)$$

where  $q_{\text{sum}}(t) = \sum_j q^j(t)$ . This  $V_{\text{sum}}(t)$  is adopted as the standard quantity representing the counting rate in the following analysis, similar to the ‘‘TDC spectrum,  $n_e(t)$ ’’ in the pulse-counting method. In the pulse-counting

method, the uncertainty associated with the TDC spectrum can be estimated based on Poisson statistics, as indicated in Eq.(6). We now estimate the uncertainty associated with the integrated voltage  $V_{\text{sum}}$  using Eq.(17). Notably, the “beam-pulse-integrated charge,  $q_{\text{sum}}$ ”, displays fluctuations,  $\sigma_{q_{\text{sum}}}$ , similar to  $Q_{\text{sum}}$ , owing to the relation  $q_{\text{sum}} = dQ_{\text{sum}}/dt$ . Thus, the uncertainty of  $V_{\text{sum}}$  can be estimated as follows:

$$\begin{aligned}
\sigma_{V_{\text{sum}}} &= \sigma_{q_{\text{sum}}} \frac{R_T}{\Delta t}, \text{ from Eq.(17)} \\
&= \sigma_{q_{\text{sum}}}^{\text{stat.}} \sqrt{1 + \hat{\sigma}_q^2} \frac{R_T}{\Delta t}, \text{ from Eq.(13)} \\
&= \sqrt{\tilde{N} Q_0} \sqrt{1 + \hat{\sigma}_q^2} \frac{R_T}{\Delta t}, \text{ from Eq.(11)} \\
&= \sqrt{\frac{q_{\text{sum}}}{Q_0}} Q_0 \sqrt{1 + \hat{\sigma}_q^2} \frac{R_T}{\Delta t}, \text{ from Eq.(12)} \\
&= \sqrt{V_{\text{sum}} \frac{\Delta t}{R_T}} Q_0 \sqrt{1 + \hat{\sigma}_V^2} \frac{R_T}{\Delta t}, \text{ from Eq.(17)} \\
&= \sqrt{(1 + \hat{\sigma}_V^2) \frac{R_T}{\Delta t}} Q_0 \sqrt{V_{\text{sum}}}. \quad (18)
\end{aligned}$$

In the above relations, we used  $\hat{\sigma}_q = \hat{\sigma}_V$  (relative uncertainty of  $V$ ) because  $V_{\text{sum}} \propto q_{\text{sum}}$ , as indicated by Eq.(17). Consequently, we obtain

$$\sigma_{V_{\text{sum}}} = \alpha \sqrt{V_{\text{sum}}} \quad (\alpha = \text{const.}). \quad (19)$$

This is similar to Eq.(14). Hence, similar to conventional counting TDC histograms, we see that the random error in the  $V_{\text{sum}}(t)$  spectrum is proportional to  $\sqrt{V_{\text{sum}}(t)}$ . The constant factor  $\alpha$  appearing in Eq.(19) can be defined using Eq.(18), as follows:

$$\alpha = \sqrt{(1 + \hat{\sigma}_V^2) \frac{R_T}{\Delta t}} Q_0. \quad (20)$$

Here,  $\alpha$  is not a dimensionless parameter but contains  $\sqrt{V}$ , where  $V$  is volt (unit). Considering that  $\hat{\sigma}_V$  is unknown, directly estimating  $\alpha$  based on the fluctuations observed in the experimental data of  $V_{\text{sum}}$  appears to be a better alternative compared to using Eq.(20). Further discussions on this aspect will be outlined in Section VI.

Note that electrical noise contributes to  $\hat{\sigma}_V$  but is included in  $\alpha$ . Importantly, the effect of electrical noise does not appear as a constant offset contribution limiting the precision; instead, it is smeared out in the averaging process over many events.

The calculations outlined in this section reveal that  $V_{\text{sum}}(t)$  is proportional to the event rate  $n_e(t)$ , while its random uncertainty is proportional to its square root.

#### IV. SIMULATION

We conducted a Monte-Carlo simulation study to demonstrate the behavior of  $V_{\text{sum}}(t)$ . Here, asymmetric Gaussian signal pulses with a rise time of 2 ns and a fall

time of 4 ns were generated. The mean peak voltage was set to 2 V, with  $\pm 0.2$  mV Gaussian fluctuations. Following this, event arrival timings were generated randomly at constant count rates of approximately (a) 10 Mcps, (b) 100 Mcps, (c) 1 Gcps, and (d) 10 Gcps. The generated pulse signals were then recorded with a sampling time step of  $\Delta t = 2$  ns.

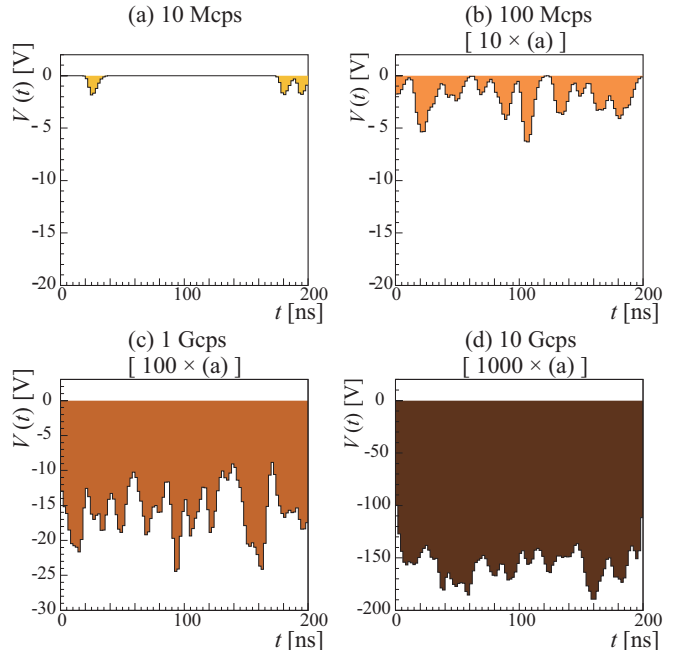


FIG. 6. Simulation results of time-sequential voltage data  $V(t)$  at different event rates.

The time-sequential voltage data,  $V(t)$ , are shown in Fig.6 (a–d). These data correspond to the input voltage signals recorded by digitizers or oscilloscopes, similar to that displayed in Fig.2. The signal pileup phenomenon may initiate from  $\sim 10$  Mcps, making individual pulses with count rates of over 1 Gcps indistinguishable.

These results can also be interpreted as (a)  $V(t)$  for a beam pulse at 10 Mcps or (b/c/d)  $V_{\text{sum}}(t)$  obtained by summing over  $N_{\text{pulse}} = 10/100/1000$  beam pulses at 10 MHz as follows:

$$V(t)^{(b/c/d)} \leftrightarrow \sum_{\text{beam pulse } j=1}^{N_{\text{pulse}}=10/100/1000} V(t)_j^{(a)}. \quad (21)$$

This demonstrates the behavior of  $V_{\text{sum}}(t) = \sum_j V_j(t)$ .

Evidently, voltage discrimination is impossible for count rates exceeding 1 Gcps owing to severe pileup phenomena. However, even before reaching this threshold, pulse identification efficiency decreases owing to counting losses resulting from two-pulse pileups. In addition to this, counting losses originate from the intrinsic deadtime of PMTs resulting from effective bias reduction and the electric deadtime attributed to the processing of downstream digital signals in the conventional pulse-counting

method utilizing discriminators. Consequently, counting losses initiate even before reaching the count rate at which signal pileup begins, which can be estimated based on the signal width.

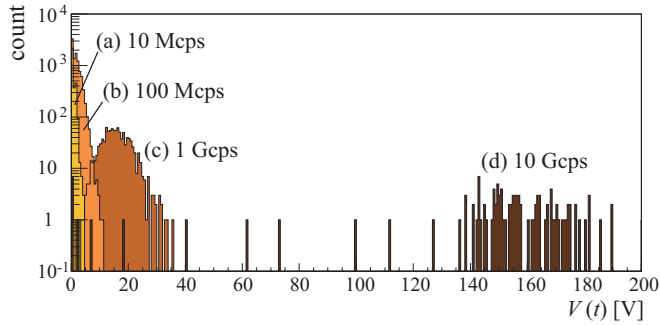


FIG. 7. Voltage distributions obtained by projecting the  $V(t)$  data plotted in Fig.6 along the voltage axis.

To examine the voltage distributions, we obtained the time-projection distributions of the profiles shown in Fig.6, and the obtained distributions are displayed in Fig.7. For case (a), the shown distribution corresponds to the voltage profile of a typical single pulse whose end-point lies at a peak voltage of 2 V. In cases (b–d), the mean voltage values increase due to signal pileups. The minimum voltage of the distributions exceeds zero, particularly for count rates exceeding 1 Gcps (c, d). This implies that the time sequence signal is consistently piled up without returning to zero, i.e.,  $V(t) > 0$  for any  $t$ . As shown in Fig.6(c,d), pulse-like structures remain even under high-counting-rate conditions, without being smeared. The amplitudes of these “pulses” can be as large as 10 V. Hence, these cannot be identified as single signal pulses, known to exhibit peak heights of  $\sim 2$  V. This unnatural behavior will be discussed in Section VI.

## V. RESULTS

### A. Charge Spectra

Fig.8(a) shows a typical output signal extracted from a PMT detecting positrons generated from the decay of stopped muons in the  $\mu$ LV-Run0 experiment. It shows the voltage pulse shape, similar to that displayed on an oscilloscope (Figs.2 and 6). A software time gate was employed in offline data analysis to perform pulse-charge measurements similar to using QDCs, as shown in Fig.8(b).

Similar to hardware discrimination, software gates were determined using leading-edge discrimination. The integrated charge within the gate was calculated as follows:

$$Q_{\text{QDC}} = -\frac{1}{R_T} \int_{\text{gate}} V(t) dt = -\frac{T_{\text{gate}}}{R_T} \sum_{k \subseteq \text{gate}} V(k\Delta t),$$

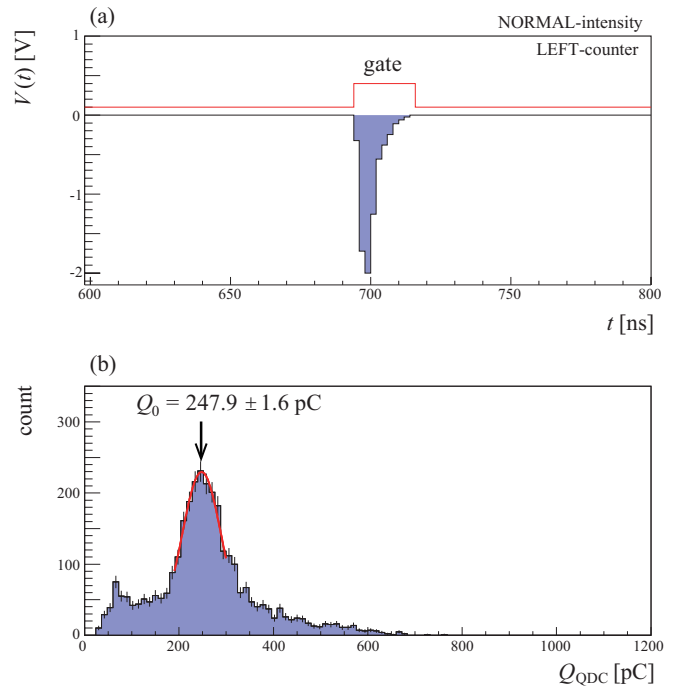


FIG. 8. Data recorded by the LEFT counter under PMT exposure to the NORMAL-intensity beam. (a) Typical  $V(t)$  of a PMT, recorded by a digitizer. (b)  $Q_{\text{QDC}}$  distribution from the “QDC” analysis.

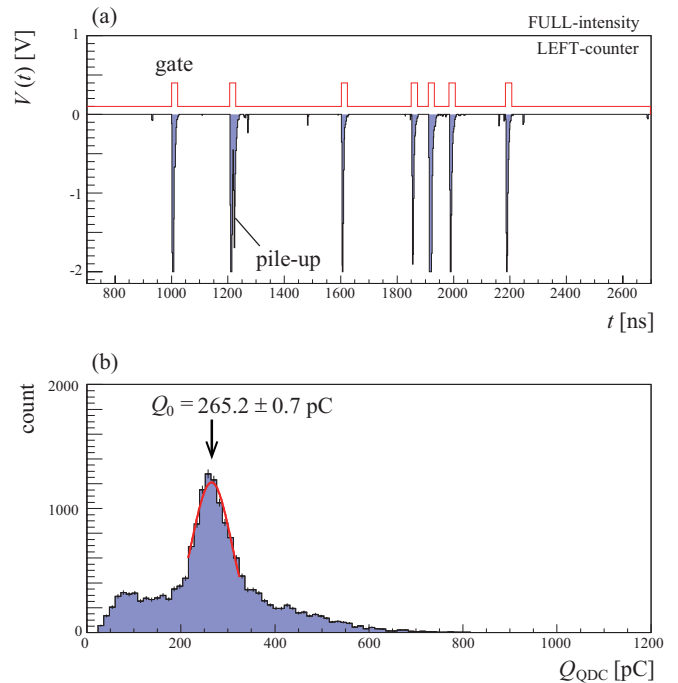


FIG. 9. Same as Fig.8 but for results for FULL-intensity beam in the LEFT counter are shown.

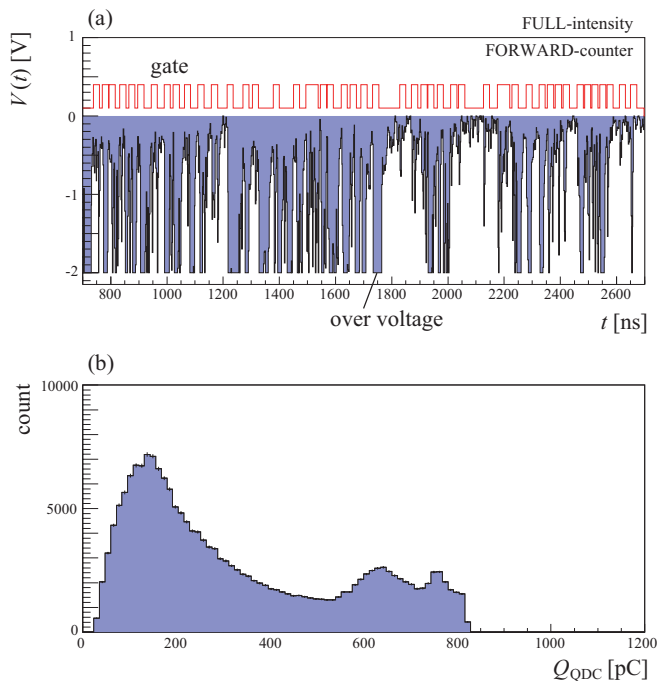


FIG. 10. Same as Fig.8 but for results for FULL-intensity beam in the FORWARD counter are shown. Severe pileups are apparent.

The distribution of this integrated charge over many events is shown in Fig.8(b). This distribution corresponds to the charge distribution derived from conventional hardware QDC measurements. The displayed profile exhibits a peak structure corresponding to the mean energy deposition within the thin plastic scintillation counter, where almost all positrons penetrate without stopping. By determining the peak position, we can estimate the average charge output derived from the PMT and flowing through  $R_T$  as  $Q_0 = 248$  pC. Based on this, we can convert the observed integrated charge  $Q$  into the equivalent pulse number,  $n_{\text{equiv.}} = \tilde{N}$  using  $Q_0$  as  $n_{\text{equiv.}} = Q/Q_0$ .

The data displayed in Fig.8 were recorded by the LEFT counter under PMT exposure to the NORMAL-intensity beam. Similar results were observed for the FULL-intensity beam, as shown in Fig.9. Although signal pileups were not apparent in this case, the pulse-to-pulse duration was sufficiently small to initiate accidental pileups. The highest event rate scenario in our data was observed in the results obtained from the FORWARD counter under exposure to the FULL-intensity beam, as shown in Fig.10. Here, we notice severe pileups, which prevent the separation of independent signal pulses. This situation roughly corresponds to the simulation result shown in Fig.6(b). Notably, the digitizer employed in the experiment has a maximum measurable voltage of 2 V, resulting in a voltage cut-off at this level. Hence, we partially lost voltage information for well-overlapping pulses. To

avoid this, the data must have ideally been recorded at  $|V| \sim 1$  V by adjusting the gain. Unfortunately, we were not fully aware of this voltage cut-off limitation during the  $\mu$ LV-Run0 experiment.

The peak value shown in Fig.9(b) is slightly larger than that shown in Fig.8(b). Consequently, the  $Q_0$  value estimated from this QDC analysis may not be adequately reliable to be treated as a constant value across different measuring conditions in subsequent data analysis.

## B. Time Spectra

The primary scientific measurement in this study focused on the time spectra of event frequency, which corresponds to the TDC histogram generated by the conventional pulse-counting method. Samples of the obtained integrated voltages,  $V_{\text{sum}}(t)$ , are shown in Fig.11, where (a, b, c) correspond to  $\tilde{N}_{\text{pulse}} = (1, 100, 500)$ , i.e., ( $T_{\text{run}} = 1/25, 4, 20$  s). Evidently, compared to the pulse signals displayed in Fig.11(a), those shown in Fig.11(b, c) demonstrate increased overlapping, forming spectra similar to conventional TDC histograms that reflect an exponential decay curve.

The results of  $V_{\text{sum}}(t)$  integrated over  $T_{\text{run}} = 1$  h each are shown in Figs.12 and 13. Fig.12 displays a decay curve, which simply represents a single exponential decay events with a constant lifetime. Fig.13 presents a  $\mu$ SR spectrum obtained by subjecting the muon stopper to a transverse (vertical) magnetic field. By fitting the obtained data, we can obtain the lifetime and spin precession frequency. These results indicate that the current-readout method is sufficiently capable of performing such scientific measurements. The time spectra shown here are plotted with error bars computed using Eq.(19) after determining  $\alpha$ . The estimation of random errors, including the determination of  $\alpha$ , will be discussed later in Section VI.

The profiles shown in both Figs.12 and 13 resemble conventional TDC histograms. However, these are not histograms but integrated voltage data. In these figures,  $\bar{V}_{\text{sum}}$  is plotted instead of  $V_{\text{sum}}$ .  $\bar{V}_{\text{sum}}$  is defined as the average value of  $V_{\text{sum}}$  over a rebinning time period of  $\Delta t_{\text{rebin}} = 20$  ns for 10 time bins. Indeed, the tail region presented in Fig.14 reveals the shapes of remaining independent pulses, which do not appear in conventional TDC histograms. This indicates that integrated voltage spectra,  $V_{\text{sum}}(t)$ , can be interpreted as averaged flux values within the high-statistics region; conversely, discrete pulses remain unsmoothed by other pulses in the low-statistics region. The counting rate shown in Fig.12 was estimated by comparing the voltage sum with the  $Q_0$  value as

$$n_{\text{LEFT}}(t=0) = \frac{\bar{V}_{\text{sum}}(t)}{\eta}, \quad \eta \equiv R_T N_{\text{pulse}} Q_0. \quad (22)$$

Using  $Q_0$ , we can estimate the absolute counting number and random errors by relying on Poisson statistics.



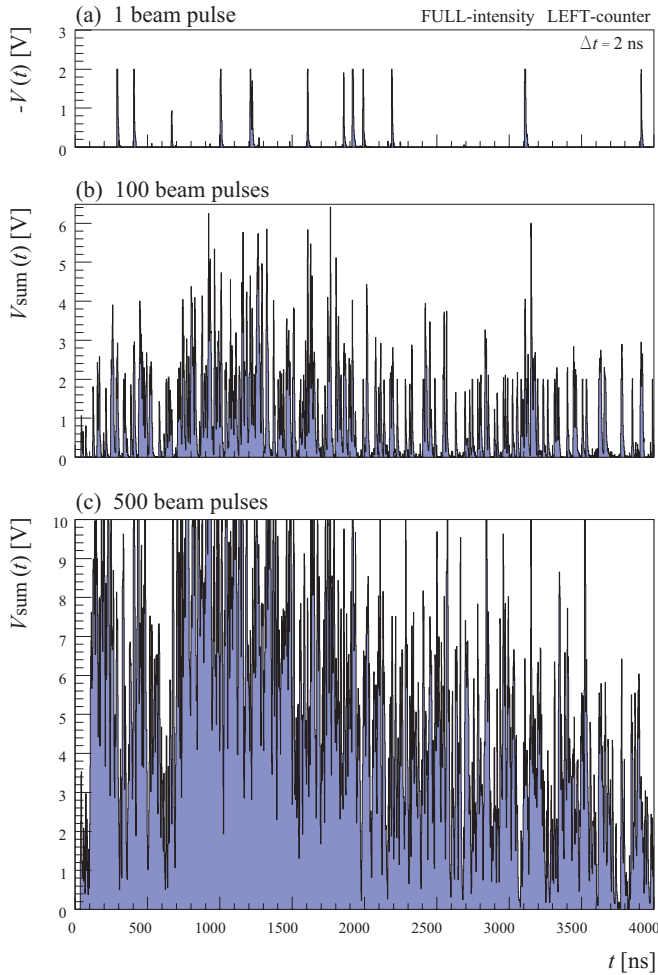


FIG. 11. Data recorded by the LEFT counter under PMT exposure to the FULL-intensity beam. (a) Sample time-sequence voltage data,  $-V(t)$ , presenting one beam pulse. Individual event pulses are isolated. (b)  $V_{\text{sum}}(t)$  integrated over 100 beam pulses. ‘‘Pileup’’ (pulse overlapping) can be observed. (c)  $V_{\text{sum}}(t)$  integrated over 500 beam pulses. ‘‘Pileup’’ events form a ‘‘decay curve.’’

However, the measured voltages may include other random fluctuation sources beyond Poisson fluctuations. A direct analysis of these random fluctuations will be detailed in the subsequent section.

### C. Random Fluctuation

The properties of the random fluctuations in  $V_{\text{sum}}$  were examined using the experimental data, and the corresponding results are shown in Fig.15. The  $\chi^2$  values plotted in this figure were estimated by performing simple exponential fitting across numerous segmented narrow regions (with a width of 200 ns) of the decay curve displayed in Fig.12. The function adopted for this expo-

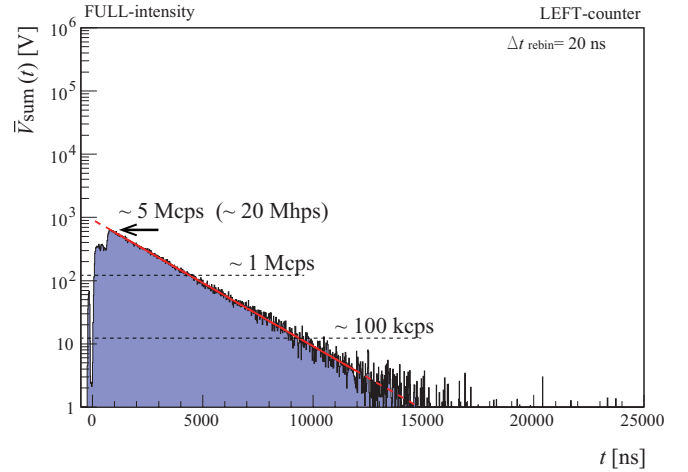


FIG. 12.  $\bar{V}_{\text{sum}}(t)$  spectrum extracted from the LEFT counter under FULL-intensity beam exposure, representing a simple exponential decay curve. The solid line indicates the fitting result obtained using the exponential function. Corresponding counting rates are also included and were estimated using the  $Q_0$  value.

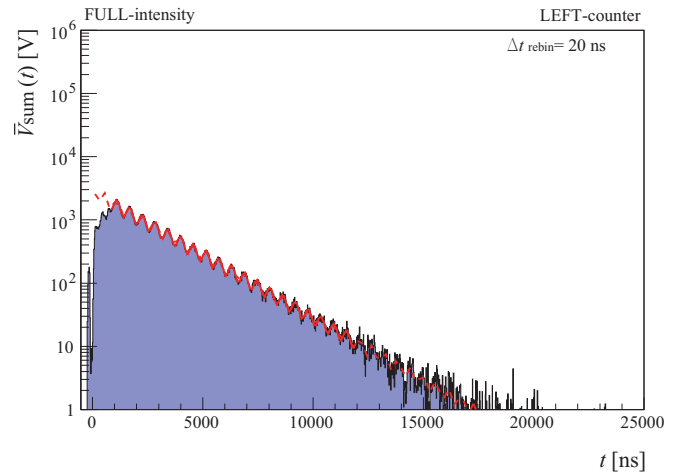


FIG. 13. Same as Fig.12, but a transverse magnetic field was applied to generate spin precession for this data. The solid line indicates the fitting result obtained using the exponential function, including spin precession, illustrated as the oscillation pattern around the exponential decay curve.

nential fitting on  $\bar{V}_{\text{sum}}$  was

$$V_{\text{model}}(t) = A \exp^{-t/\tau_{\mu}}. \quad (23)$$

Initially, a two-parameter ( $A, \tau_{\mu}$ ) fitting was performed over a wide region of the decay curve displayed in Fig.12 without segmenting it. Subsequently, narrow window fittings were performed on segmented decay curves, fixing the value of the lifetime parameter obtained above and setting the scale parameter,  $A$ , as the free parameter.

The number of independent data points within the segmented 200-ns-fitting region was 10, yielding a degree of

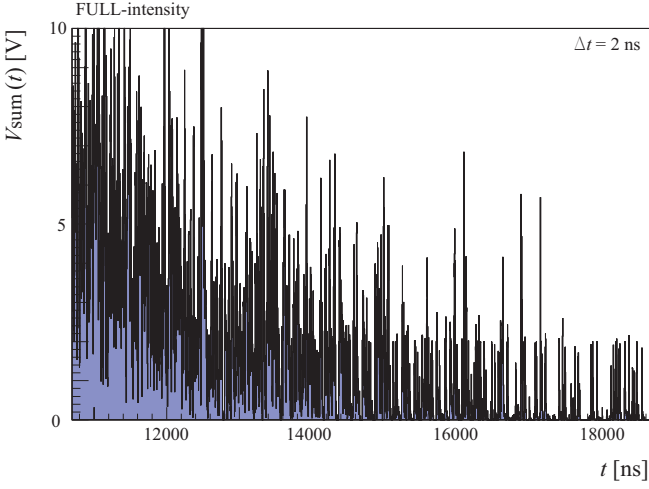


FIG. 14. Same as Fig.11 but showing a different  $t$  region. Independent event pulses at  $t \sim 18,000$  ns are apparent; however, their pileup begins forming a decay curve structure at  $t \sim 12,000$  ns.

freedom of  $n_{\text{ndf}} = 10 - 1 = 9$  for the fitting. The obtained result shown in Fig.15 demonstrates excellent agreement with the expected  $\chi^2$  distribution with the parameter  $\nu = n_{\text{ndf}}$ :

$$P_\nu(\chi^2) = \frac{(\chi^2/2)^{\nu/2-1} e^{-\chi^2/2}}{2\Gamma(\nu/2)}. \quad (24)$$

This implies that the fluctuation  $\sigma_{V_{\text{sum}}}$  used to estimate  $\chi^2$  values obeys a Gaussian distribution, allowing reliable model fitting using conventional  $\chi^2$  minimization.

To obtain the results and perform this  $\chi^2$  analysis, we determined the random error  $\sigma_{V_{\text{sum}}}$  in the experimental data  $V_{\text{sum}}$ :

$$\chi^2 = \sum_{\text{data } K} \left( \frac{\bar{V}_{\text{sum}}(K\Delta t_{\text{rebin}}) - V_{\text{model}}(K\Delta t_{\text{rebin}})}{\sigma_{V_{\text{sum}}}(K\Delta t_{\text{rebin}})} \right)^2, \quad (25)$$

where  $K$  denotes the number like  $k$ , but of the rebinned data  $\bar{V}_{\text{sum}}$ , i.e.,  $t = K\Delta t_{\text{rebin}}$ .

The value of  $\alpha$  in Eq.(19) was determined to reproduce the  $\chi^2$  distribution corresponding to  $n_{\text{ndf}}$  by ensuring agreement between the data and model, as shown in Fig.15. Initially, the  $\chi^2$  distribution was generated using a temporary value of  $\alpha_{\text{temp.}} = 1\sqrt{V}$ . Subsequently, the optimized  $\alpha$  was approximately obtained using the mean value  $\langle \chi_{\text{temp.}}^2 \rangle$  of the  $\chi^2$  distribution utilizing  $\alpha_{\text{temp.}}$ , as follows:

$$\alpha = \sqrt{\frac{\langle \chi_{\text{temp.}}^2 \rangle}{n_{\text{ndf}}}}. \quad (26)$$

This is because  $\langle \chi_{\text{temp.}}^2 \rangle / \alpha^2 = \langle \chi^2 \rangle = n_{\text{ndf}}$ . Thus, we determined  $\alpha$  by estimating the fluctuation in the experimental data, instead of using Eq.(20). From this analysis,

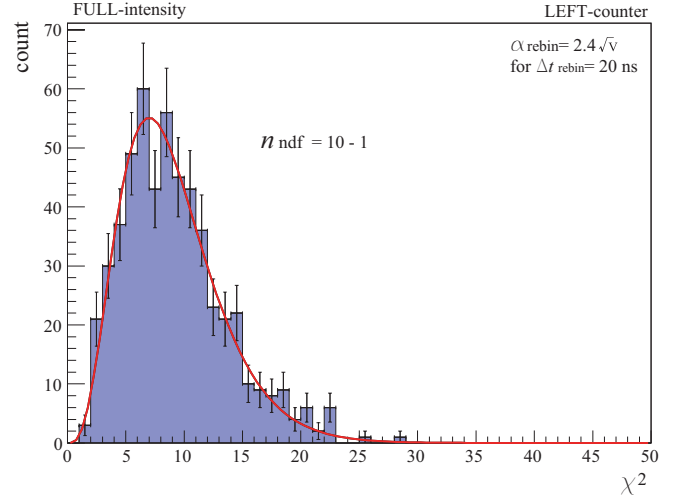


FIG. 15. Distribution of  $\chi^2$  values obtained from the fine-segmented exponential decay curve, as will be described in Section VIA using Fig.17. Ten points were used for the fitting. The error associated with each data point was evaluated using Eq.(19), with  $\alpha_{\text{rebin}} = 2.4\sqrt{V}$ . By properly tuning this  $\alpha$  value, the obtained distribution demonstrated good agreement with the theoretical  $\chi^2$  distribution, with  $n_{\text{ndf}} = 10 - 1$ , indicated by the solid line.

we determined the  $\alpha$  factor as  $\alpha_{\text{rebin}} = 2.4\sqrt{V}$  for the rebinned data by performing fine-tuning in accordance with Fig.15.

The abovementioned agreement with the  $\chi^2$  distribution suggests the Gaussian properties of the fluctuations in  $V_{\text{sum}}$ , which can be directly tested by examining the fluctuating  $V_{\text{sum}}$  distribution itself. As shown in Fig.5, we identified a time window  $T_w$  to obtain the time-integrated charge for the  $j$ -th beam pulse as follows:

$$Q_j^w = \sum_k^{k\Delta t \leq T_w} q_j(k\Delta t) = - \sum_k^{k\Delta t \leq T_w} \frac{V_j(k\Delta t)\Delta t}{R_T}. \quad (27)$$

Following this, the  $Q_j^w$  distribution over different beam pulses,  $j$ , was examined, as shown in Fig.16. In this figure, cases (A/B/C/D/E) show the results summing  $N_{\text{pulse}} = 1/10/20/40/60$  beam pulses, i.e.,

$$Q_{\text{sum}}^{w(A/B/C/D/E)} = \sum_j^{j \leq 1/10/20/40/50} Q_j^w. \quad (28)$$

For case (A), the integrated charge distribution displayed peaks at  $Q_{\text{sum}}^{w(A)} \sim Q_0, 2Q_0, 3Q_0$ , as presented in Fig.16(a). Using the  $Q_0$  value in Eq.(9),  $n_{\text{equiv.}} = Q_w/Q_0$  (number of event pulses included in  $T_w$ ) was estimated, as plotted along the upper horizontal axis. Indeed, three peaks were observed at the  $n_{\text{equiv.}} = 0, 1, 2, 3$  positions. For cases (B–E), the distribution displayed in Fig.16(b) exhibits peaks at  $Q_{\text{sum}}^w \sim 10Q_0, 20Q_0, 40Q_0, 60Q_0$ , corresponding to  $n_{\text{equiv.}} \sim 10, 20, 40, 60$ , respectively.

These results were then compared with the theoretical Poisson distribution. The solid lines in the figures show the corresponding Poisson distributions, with parameter  $m$  indicating the expected value of the distribution. Here, we used a continuum function to generate the Poisson distribution by extending the functional form using an integer variable  $\kappa$  to that using a real number variable  $x$  as follows:

$$P_m(\kappa) = \frac{m^\kappa}{\kappa!} e^{-m} \quad (\kappa \in \text{integer} \geq 0) \quad (29)$$

$$\rightarrow P_m(x) = \frac{m^x}{\Gamma(x+1)} e^{-m} \quad (x \in \text{real number} \geq 0). \quad (30)$$

The data and model demonstrated good agreement, indicating that the integrated charge obeys the Poisson distribution. This suggests that the integrated voltage  $V_{\text{sum}}$  exhibits Poisson fluctuations, which converge to Gaussian fluctuations, corroborating the error estimation accomplished using  $\sqrt{V_{\text{sum}}}$  in Eq.(19).

We confirm that the fluctuation properties satisfy the requirement for the application of the conventional  $\chi^2$  analysis, which assumes Gaussian fluctuations of the random errors of data points.

## VI. DISCUSSION

### A. Random Error Estimation

Using the obtained experimental data, our next analysis focuses on examining the square-root property of Eq. (19). As detailed in Section V C, we performed  $\chi^2$  fittings on the fine-segmented regions of the decay spectra to extract the  $\chi^2$  distribution displayed in Fig.15. During this process, the standard deviations,  $\sigma_{V_{\text{sum}}}$ , of the data distributed around the fitted curves were calculated while determining the  $\chi^2$  value.

Fig.17 shows the process of segmented fitting. Specifically, we performed simple exponential fitting in narrow segmented regions with a width of 200 ns, as shown in Fig.17(a), and repeated the process by shifting the fitting region to different  $t$  values. Fig.17(b,c) presents an enlarged view of the fitting region for (b) the original data with a bin width of  $\Delta t = 2$  ns and (c) rebinned data with a bin width of  $\Delta t_{\text{rebin}} = 20$  ns. Fig.17(a,b) presents the  $V_{\text{sum}}$  distribution, while Fig.17(c) shows the distribution of  $\bar{V}_{\text{sum}}$ .

The numbers of data points included within the regions shown in Fig.17(b) and (c) are  $N_{\text{dat}} = 100$  and  $N_{\text{dat}} = 10$ , respectively, owing to the rebinning. The vertical error bars shown in Fig.17(b) were estimated using Eq.(19), assuming a tentative value of  $\alpha = \alpha_{\text{temp.}} = 1 \times \sqrt{V}$ . The  $\alpha$  value corresponding to the data in Fig.17(c) ( $\alpha_{\text{rebin}}$ ) was independently evaluated by ensuring that the  $\chi^2$  distribution for the rebinned data remained consistent with

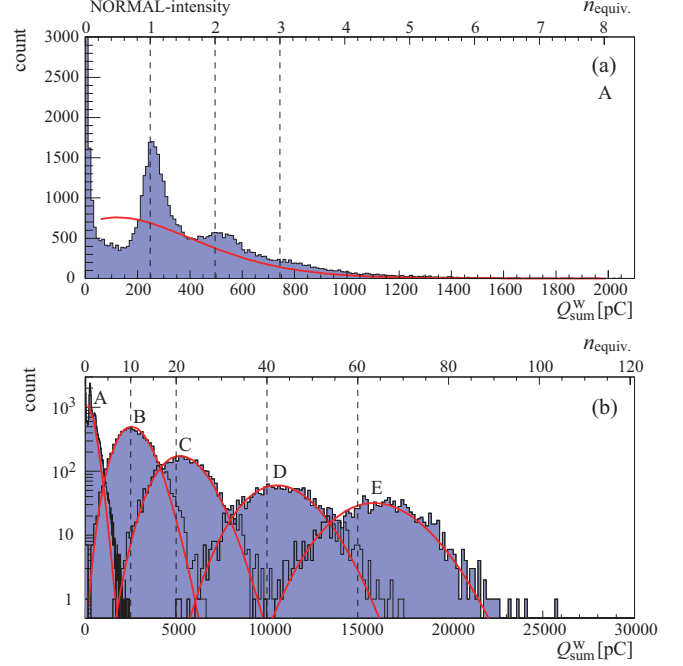


FIG. 16. Distribution of  $Q_{\text{sum}}^w$  defined in Eq. (28). (a) and (b) are similar but show different  $Q_{\text{sum}}^w$  regions. The upper horizontal axis represents the equivalent counting number,  $n_{\text{equiv.}}$  estimated using the value of  $Q_0$ . The  $Q_{\text{sum}}^w$  distributions, obtained by tuning the expected value  $m$  defined in Eq.(30) in the  $n_{\text{equiv.}}$  spectra, demonstrate good agreement with the Poisson distributions. Refer to the main text for details on the  $N_{\text{pulse}}$  settings for cases A/B/C/D/E defined in Eq.(28).

the theoretically expected  $\chi^2$  distribution, as detailed in Section V C.

Fig.17(c) displays two different error bars. One type was estimated using  $\alpha_{\text{temp.}}$  represented using black boxes, while the other was estimated using  $\alpha_{\text{rebin}}$ , indicated as solid lines. The fluctuation observed in Fig.17(b) is natural because the fitting result of  $\chi^2/\text{ndf} = 88.1/99$  using  $\alpha_{\text{temp.}}$ . This indicates that the tentative selection of  $\alpha_{\text{temp.}} = 1$  was accidentally adequate. However, for the rebinned data displayed in Fig.17(c), we note that the fluctuation around the fitted line becomes excessive if we use the assumed value of  $\alpha_{\text{temp.}}$ . Indeed,  $\chi^2/\text{ndf} = 37.05/9$  for  $\alpha_{\text{temp.}}$  becomes excessively large, while  $\chi^2/\text{ndf} = 6.63/9$  for  $\alpha_{\text{rebin}}$  remains adequate. This implies that the  $\alpha$  estimation based on Eq.(26) adequately computes the random uncertainty. If statistical errors are treated appropriately,  $\alpha$  values must not depend on the binning selection. The reason underlying the difference between  $\alpha_{\text{temp.}}$  and  $\alpha_{\text{rebin}}$  values will be discussed in Section VI B.

After performing the fittings, the standard deviations,  $\sigma_{V_{\text{sum}}}$ , were estimated as the fluctuations around the fitted curve,  $V_{\text{model}}$ , for each segmented fitting region, as

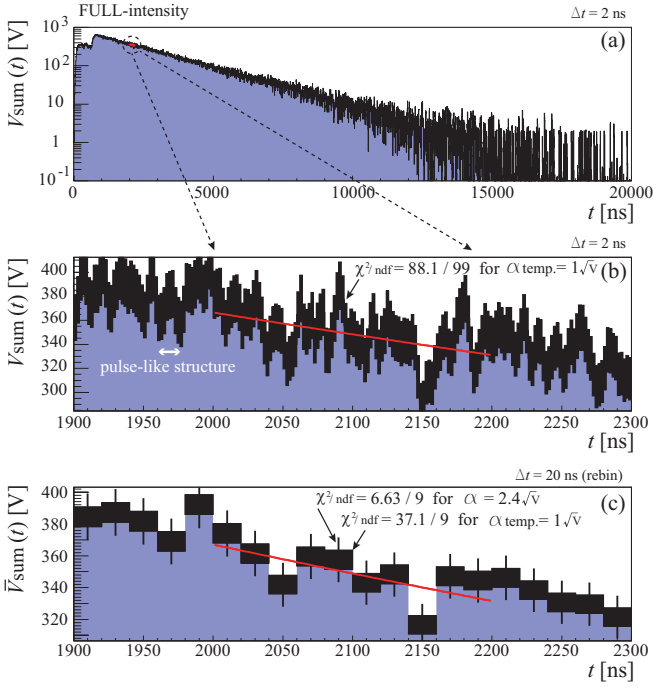


FIG. 17. Fine-segmented fitting performed using a single exponential function. Solid lines indicate the fitted results. (a)  $V_{\text{sum}}(t)$  spectrum with  $\Delta t = 2$  ns, i.e., without rebinning. An example of the fitting region is also shown. (b) Enlarged view of (a) around the fitting region. Error bars were estimated using  $\alpha_{\text{temp}} = 1$ . (c) Rebinned results representing  $\bar{V}_{\text{sum}}(t)$ . Average voltages are shown instead of summing  $V_{\text{sum}}(t)$  across 10 time bins. Two types of error bars are shown, corresponding to  $\alpha_{\text{temp}} = 1\sqrt{V}$  (box) and  $\alpha_{\text{rebin}} = 2.4\sqrt{V}$  (bar), respectively.

follows:

$$\sigma_{V_{\text{sum}}}^2 = \frac{1}{N_{\text{dat}} - 1} \sum_{k=1, N_{\text{dat}}} (V_{\text{sum}}(k\Delta t) - V_{\text{model}}(k\Delta t))^2, \quad (31)$$

where  $k = 1 \dots N_{\text{dat}}$  denote the number of data within the fitting region. Similarly, the standard deviations for the rebinned data,  $\sigma_{\bar{V}_{\text{sum}}}$ , were also estimated. Subsequently, datasets of  $(V_{\text{sum}}, \sigma_{V_{\text{sum}}})$  and  $(\bar{V}_{\text{sum}}, \sigma_{\bar{V}_{\text{sum}}})$  for the numerous fitting regions were obtained. Figs.18 and 19 show their correlations.

By examining these correlations, we can directly test Eq.(19). The horizontal errors of  $V_{\text{sum}}$  shown in Fig.18 were estimated as their standard errors  $\sigma_{V_{\text{sum}}}/\sqrt{N_{\text{dat}}}$ . The vertical errors of  $\sigma_{V_{\text{sum}}}$  were estimated as the standard errors of standard deviation as  $\sigma_{\sigma_{V_{\text{sum}}}} = \sigma_{V_{\text{sum}}}/\sqrt{2(N_{\text{dat}} - 1)}$ . The errors presented in Fig.19 were estimated in the same manner.

The results shown in both figures are consistent with the slope indicating  $\sigma \propto V_{\text{sum}}^{0.5}$ . Once again, we successfully confirm the square-root property of Eq.(19). We performed fittings on the  $(V, \sigma)$  correlations by setting  $\alpha'$  as the parameter to be optimized, yielding  $\alpha' = 1.0\sqrt{V}$

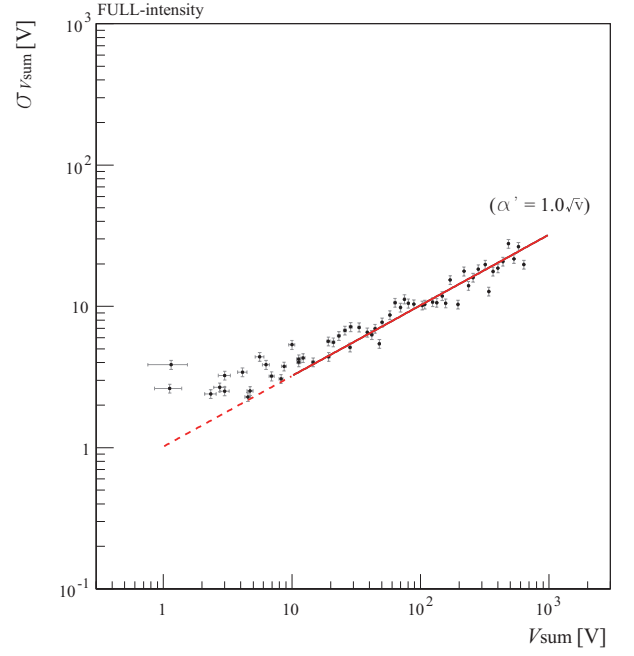


FIG. 18.  $(V_{\text{sum}}, \sigma_{V_{\text{sum}}})$  correlation fitted using Eq.(19). The obtained result is consistent with the square-root property.  $\alpha$  value obtained as the fitting result is  $\alpha'$ . The dotted region was not included in the fitting because individual event pulses dominated the spectrum.

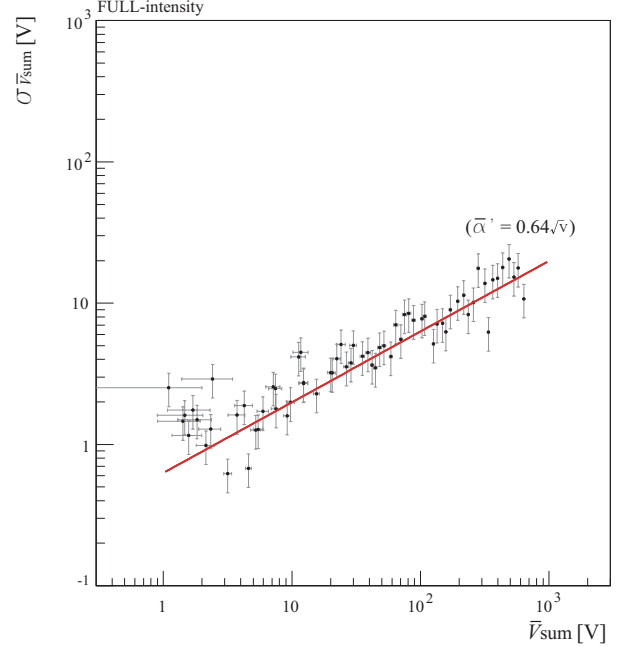


FIG. 19.  $(\bar{V}_{\text{sum}}, \sigma_{\bar{V}_{\text{sum}}})$  correlation for the rebinned data fitted using Eq.(19). The obtained result is consistent with the square-root property.  $\alpha$  value obtained as the fitting result is shown as  $\bar{\alpha}'$ . The entire  $\bar{V}_{\text{sum}}$  region was involved in the fitting, in contrast to Fig.18, owing to the increased statistics resulting from the rebinning of smeared event pulses.

and  $\overline{\alpha'} = 0.64\sqrt{V}$ . The differences in the obtained  $\alpha'$  values which are shown in Figs.18 and 19 correspond to the differences between  $\alpha_{\text{temp}}$  and  $\alpha_{\text{rebin}}$ , as evident from Fig.17. The result  $\alpha' \sim \alpha_{\text{temp}}$  implies that the tentative assumption of  $\alpha_{\text{temp}} = 1\sqrt{V}$  was accidentally adequate, as observed in Fig.17(b).

As the random fluctuation is suppressed by considering mean values,  $\sigma_{\overline{V}_{\text{sum}}} \sim \sigma_{V_{\text{sum}}}/\sqrt{10}$ . This occurs because we combine 10 independent data points into one bin during the rebinning process. The obtained fitting results for  $\overline{\alpha'}$  are consistent with those for  $\alpha_{\text{rebin}}$  because  $\overline{\alpha'} \sim \alpha_{\text{rebin}}/\sqrt{10}$ . This difference arises from the distinct definitions of these parameters. For instance,  $\alpha_{\text{rebin}}$  was used before rebinning, following which  $\sigma_{\overline{V}_{\text{sum}}}$  was estimated using Eq.(19) through error propagation. Meanwhile,  $\overline{\alpha'}$  was estimated using the data obtained after rebinning. Either  $\overline{\alpha'}$  or  $\alpha_{\text{rebin}}$  can be used for the analysis; however, estimating  $\overline{\alpha'}$  might be simpler.

Thus, this section confirmed the square-root properties for both Figs.18 and 19, directly verifying the relation in Eq.(19). The parameter  $\alpha$  can be determined either by reproducing the appropriate  $\chi^2$  distribution, as shown as  $\alpha_{\text{rebin}}$  in Fig.15, or utilizing the  $\overline{V}_{\text{sum}}\text{-}\sigma_{\overline{V}_{\text{sum}}}$  correlation as  $\alpha_{\text{rebin}} \sim \overline{\alpha'}\sqrt{10}$ , as displayed in Fig.19. In the following study, we will use the  $\alpha_{\text{rebin}}$  determined from the  $\chi^2$  distribution, as described in Section 5.3, to perform  $\chi^2$  analysis. It is because it should be better to directly confirm the  $\chi^2$  distribution to perform the  $\chi^2$  fitting.

## B. Pulse-Like Structure

One may notice that the fluctuation appearing in Fig.17(b) is unnatural. Indeed, the pulse-like structure does not appear to be random fluctuations. If these fluctuations were, in fact, random and uncorrelated with different time-bin data, the scale parameter  $\alpha$  would remain constant regardless of the binning settings, i.e.,  $\alpha_{\text{temp}}$  would match  $\alpha_{\text{rebin}}$ . For conventional pulse-counting TDC histograms, the Poisson error is estimated as  $\sigma_n = \alpha_{\text{Poisson}}\sqrt{n} = \sqrt{n}$  (where  $n$  is the number of counts), implying that  $\alpha_{\text{Poisson}} = 1$  independent of binning settings. The presence of pulse-like structures indicates the existence of correlations between adjacent time bins, suggesting that different time-bin data,  $V_{\text{sum}}(t)$ , are not independent.

Similar pulse-like structures were also obtained from simulations, as shown in Fig.6, suggesting that bin-to-bin correlated fluctuations do not originate from hardware factors such as baseline fluctuations, bias power instabilities, or timing jitter of the trigger signal but are rather inherent to the mathematical method.

As we saw in Fig.17(c), the fitting  $\chi^2$  value becomes excessively large when using  $\alpha_{\text{temp}}$  to estimate the errors of the rebinned data. Adopting an alternative approach, we now assume that the estimated error bars displayed in Fig.17(b) must be excessively small, i.e.,

$\alpha_{\text{temp}}$  must be too small to obtain an adequate value. Indeed, a larger value of  $\alpha_{\text{rebin}}$  well reproduces the actual fluctuation. Thus, owing to bin-to-bin correlations, the fluctuation was estimated to be small. Given that the observed pulse-like structures demonstrate similar values across adjacent bins, the standard deviation  $\sigma_{V_{\text{sum}}}$  can be interpreted to decrease.

This unnatural correlation can be understood based on the relation between the event-pulse width  $T_{\text{pulse}} \sim 10$  ns and the sampling time bin  $\Delta t = 2$  ns as  $T_{\text{pulse}} > \Delta t$ . Owing to this wide pulse width, charges originating from the same radiation event are distributed across multiple ( $\sim T_{\text{pulse}}/\Delta t$ ) sampling time bins, leading to the persistence of the bin-to-bin correlation within a time scale of  $T_{\text{pulse}}$ .

As outlined in Section V C, although the voltage fluctuation may obey Poisson statistics, the data points cannot be treated as independent samples. Independence between data points is essential for performing  $\chi^2$  analysis. Consequently, the  $\chi^2$  values obtained without accounting for this behavior are unreliable.

Additionally, the fine time structure apparent within the time scale of  $T_{\text{pulse}}$  does not accurately represent the time structure of the real event rate. To avoid such confusion, we must ignore the fine time structure within  $T_{\text{pulse}}$ . Consequently, we applied a 10-bin rebinning procedure, wherein the time width was selected to be  $\Delta t_{\text{rebin}} \geq T_{\text{pulse}}$ , effectively filtering out high-frequency components.

Figs.12 and 13 show the rebinned ( $\Delta t_{\text{rebin}} = 20$  ns)  $\overline{V}_{\text{sum}}$  spectra facilitating reliable  $\chi^2$  fitting analysis. Conversely, Fig.14 plots the corresponding data without rebinning ( $\Delta t = 2$  ns) to show the single pulse structure in the tail region.

Thus,  $V_{\text{sum}}$  is proportional to the positron flux, and its random fluctuations obey a Poisson distribution. However, for reliable  $\chi^2$  analysis, time bins must be rebinned within  $T_{\text{pulse}}$ .

## C. Saturation

The primary objective of this study is to overcome counting saturation encountered during high-event-rate measurements. Notably, the results shown in Fig.12 can be fitted using a single exponential decay curve, indicating negligible saturation effects. The maximum counting rate of the LEFT counter was  $n_{\text{LEFT}} \sim 5$  Mcps, thus establishing a reliable upper limit for this method. Fig.12 indicates a maximum hitting rate of 20 Mhps (Mega hit/s), deduced from the beam intensity and detector acceptance, indicating differences in detector efficiency.

To benchmark this rate capability, we compared it with those of other devices using voltage discrimination. Fig.20 shows the TDC spectra recorded by Kalliope, with a solid angle per channel of  $\Omega_{\text{Kalliope}}/\Omega_{\text{LEFT}} = 0.86$  for the LEFT counter. These spectra were recorded for the same muon beam over  $T_{\text{run}}$  as the data shown in Fig.12

under FULL-intensity beam exposure. Although each segment channel of Kalliope has  $\Omega_{\text{Kalliope}}$  acceptance, the statistics shown in Fig.20 include contributions from all  $N_{\text{double}} = 640$  channels, justifying the higher statistics in Fig.20 compared to those in Fig.12.

Notably, Kalliope exhibits apparent event-number saturation at a counting rate of  $\sim 1$  Mcps per channel. The expected hitting rates shown in the figure were obtained by estimating the detection efficiency based on the coincidence rate between two layers (refer to Appendix A for details), thus concluding that our new system is more robust in terms of rate capabilities.

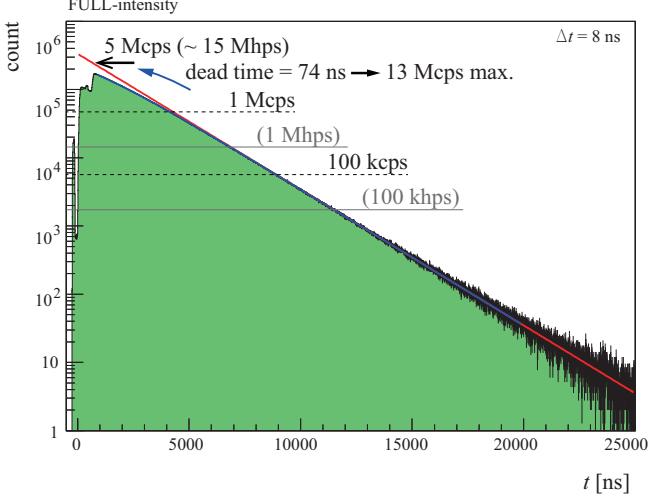


FIG. 20. Decay curve spectrum recorded by Kalliope under FULL-intensity beam exposure. “hps” indicates hits per second, evaluated based on the single hit rate of the scintillators. “cps” indicates accepted coincidence counts between the inner and outer layers per second. Their difference comes from coincidence efficiency.

The FORWARD counter was instrumental in determining the maximum event rate of our system, primarily influenced by the substantial background radiation from the beam upstream. The primary types of background radiation expected at the FORWARD counter included positrons emitted from muons decaying upstream of the stopper. Consequently, their decay curves mirrored those derived from the muons stopped at the stopper. The LEFT and RIGHT counters were almost insensitive to these radiation types owing to their setting angles and the use of radiation protection shields upstream of the detector.

The results shown in Figs.21 and 22 indicate a small saturation at  $\sim 100$  Mcps. Fig.10 corresponds to this situation. The counting rates for the FORWARD counter shown in these figures were evaluated by assuming same  $Q_0$  value determined for the LEFT counter with Eq.(22). In this sense, these results demonstrate the current driving and counting-rate-measuring capabilities of the LEFT counter.

The spin precession amplitude displayed in Fig.22

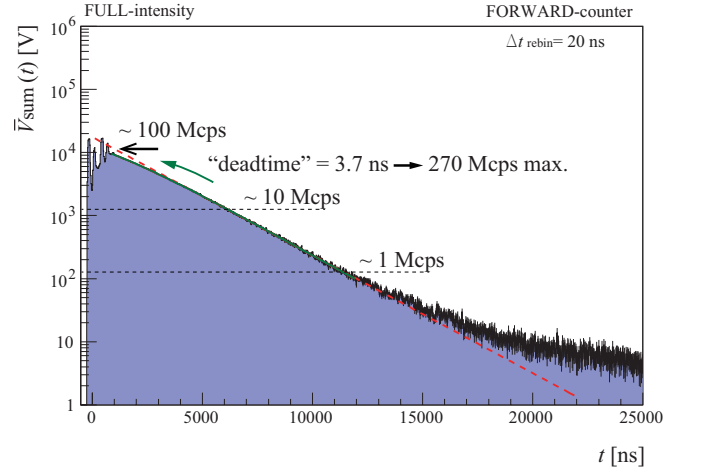


FIG. 21. Same as Fig.12, but related to the FORWARD counter. Deviations from the single exponential fitted line are apparent. Based on these deviations, the effective dead-time parameter,  $d$ , was estimated using Eq.(32). There is a component with a time constant of  $\sim 10 \mu\text{s}$ . Although the origin of this long tail component remains unidentified, muon decay can be effectively ruled out as a potential source.

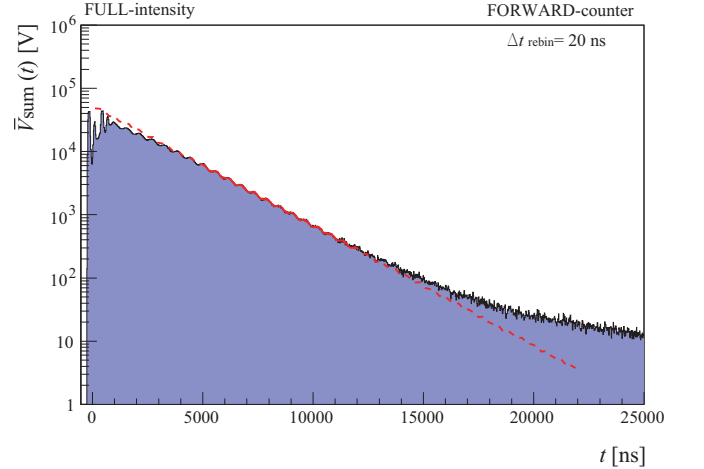


FIG. 22. Same as Fig.21, but a transverse magnetic field was applied to generate spin precession for the displayed data. The solid line indicates the fitting result obtained using the exponential function, including spin precession, illustrated as the oscillation pattern around the exponential decay curve.

is smaller than that in Fig.13. This is because most positrons hitting the FORWARD counter do not originate from the stopper, where the transverse magnetic field was applied.

Ideally, the current-readout method must not involve any real “deadtime.” Potential reasons for the saturation may include the saturation of PMTs or the voltage cut-off at 2 V, as shown in Fig.10.

Although this saturation effect does not originate from the deadtime of the electronics equipment, the data can

be well reproduced using the constant deadtime function as follows:

$$n_{\text{accept}} = \frac{1}{1/n_{\text{request}} + d}, \quad (32)$$

where  $n_{\text{accept}}(n_{\text{request}})$  denotes the accept (request) rate, and  $d$  represents the deadtime. Using this functional form,  $d = 74$  ns is obtained for the Kalliope, as shown in Fig.20. Meanwhile,  $d = 3.7$  ns is obtained for the FORWARD counter, as shown in Fig.21. It was obtained in  $\bar{V}_{\text{sum}}(t)$  fitting with Eqs.(22) and (32).

To examine the origin of the observed saturation, we performed another measurement through a different beam experiment,  $\mu$ LV Run-1, considering the inadequate gain setting of the PMTs for the data shown in Fig.21. The  $\mu$ LV-Run1 experiment was performed after the first  $\mu$ LV-Run0 experiment, under nearly identical conditions. In particular, for the new experiment, we performed a similar test measurement by setting a lower bias voltage from 1800 V to 1400 V and using a voltage attenuator to reduce the pulse height to  $\sim 200$  mV. The corresponding result is shown in Fig.23.

Although the maximum rate was not as high as that displayed in Fig.21, no visible saturation could be observed up to at least 90 Mcps. The slight saturation apparent in Fig.21 can be mitigated by reducing the bias voltage of the PMT and/or attenuating the output signals.  $d < 700$  ps was obtained by a fitting using Eq.(32) for this case.

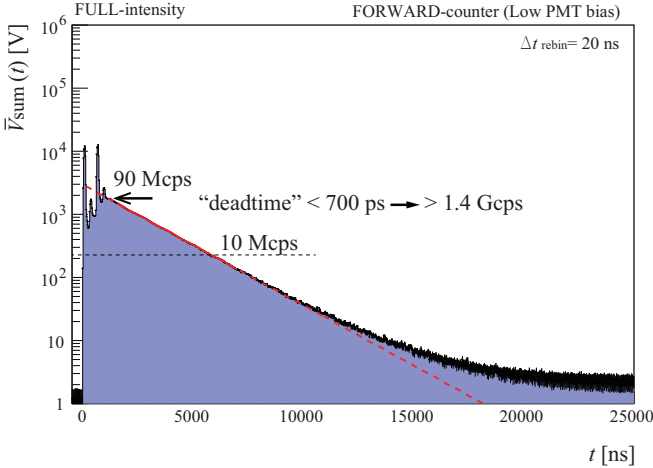


FIG. 23. Same as Fig.21 but corresponding to the  $\mu$ LV Run-1 experiment, which involved a lower PMT bias voltage and an voltage attenuator. No saturation effect is apparent.

Using Eq.(32), we can estimate the maximum event rate that can be counted. If we define the maximum acceptable counting rate as the rate when 50% of the hit events are rejected, i.e.,  $n_{\text{accept}} = n_{\text{request}}/2$ , the maximum rate  $n_{\text{request}}^{\text{max}}$  can be estimated as follows:

$$n_{\text{accept}} = n_{\text{request}}^{\text{max}}/2 = \frac{1}{1/n_{\text{request}}^{\text{max}} + d}, \quad (33)$$

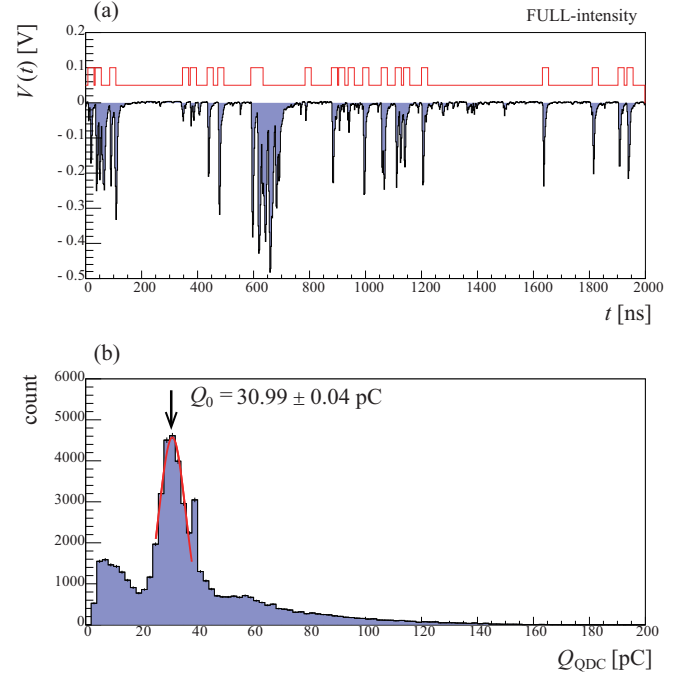


FIG. 24. Same as Fig.10 but corresponding to the  $\mu$ LV Run-1 experiment, involving a lower PMT bias voltage and a voltage attenuator. (a) The voltage saturation at 2 V is avoided. (b) Smaller  $Q_0$  value is confirmed.

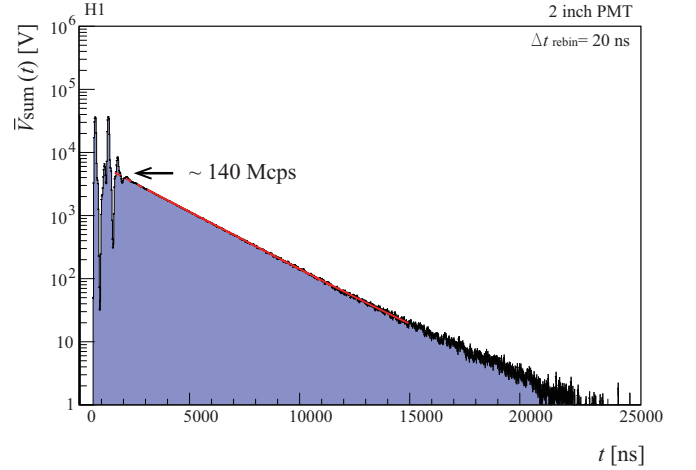


FIG. 25. Same as Fig.21 but corresponding to the measurement at H1 area. No saturation effect is apparent.

which yields

$$n_{\text{request}}^{\text{max}} = 1/d. \quad (34)$$

Then,  $n_{\text{request}}^{\text{max}} = 1/(3.7 \text{ ns}) \rightarrow 270$  Mcps is expected in Fig.21 obtained in the setting of  $\mu$ LV-Run0. From the result in Fig.23 for  $\mu$ LV-Run1 by reducing the PMT's HV setting,  $n_{\text{request}}^{\text{max}} > 1/(700 \text{ ps}) \rightarrow 1.4$  Gcps was obtained. Fig.24 shows the signal pulses and the QDC

spectrum, showing no voltage saturation and a small  $Q_0$  value due to a lower HV setting. Finally, we performed an additional measurement at the H1 area [11], where a much stronger beam was available than the D1 area at J-PARC MLF. We set the LEFT counter using 2-inch PMT (Hamamatsu H7195, plus 51mm diameter, thickness of 0.5 mm BC408 plastic scintillator) this time, 600 mm apart from the center of the aluminum beam stopper. Its result is shown in Fig.25, indicating 140 Mcps counting rate at the maximum with negligible saturation, promising  $n_{\text{request}}^{\text{max}} > 1$  Gcps.

In summary, the proposed method is anticipated to allow  $>1$  Gcps measurements if the output voltage is within the digitizer's acceptable range and if the PMT does not saturate.

#### D. PMT's Saturation

To test the saturation of the PMTs, we performed a dedicated offline measurement using a light-emitting diode (LED) to illuminate the photocathode. Specifically, a blue LED was placed within the LEFT counter to emit visible light. The input voltage for the LED driver was a rectangular pulse with a width of  $2 \mu\text{s}$  and height of  $V_{\text{LED}} = 1.2 \text{ V}$ , as shown in Fig.26. By adjusting  $V_{\text{LED}}$ , we could vary the amount of light hitting the PMT. The output signal of the PMT subjected to a voltage bias of 1800 V observed using  $R_{\text{T}} = 50 \Omega$  termination is also shown, and its shape differs from that of the input light signal.

The anode of the PMT was terminated using an internal resistor with a resistance of  $50 \Omega$ . Notably, the charge measured in the previous experiments corresponds to the current flowing through  $R_{\text{T}}$ . To estimate the total charge generated within the PMT, we must consider the total resistance as  $25 \Omega$ .

From the obtained result, the maximum charge of the PMT over a short period on the order of  $\sim \mu\text{s}$  is  $Q_{\text{saturation}} \sim 100 \text{ nC}$ . For larger amounts of charge, the signal output must be suppressed. The saturated event number is roughly estimated as  $n_{\text{saturation}} = Q_{\text{saturation}} / (Q_0 \times 50\Omega / 25\Omega) \sim 200$  events/beam pulse if photoelectrons arrive at the PMT as a continuous current.

In practical situations, input photoelectrons arrive in the form of pulse-like currents. Therefore, the saturation effect may be mitigated over the event-off timing. The small saturation of  $V_{\text{sum}}$  observed in Fig.21 might be partially attributed to this saturation of the PMT.

When using a large number of PMTs, the power stability of high-voltage power supplies must be considered. One approach to avoid the saturation and bias power instabilities of PMTs involves reducing the bias voltage. However, reducing the bias voltage or usage of voltage attenuation may exacerbate output charge fluctuations, i.e.,  $\sigma_V$ .

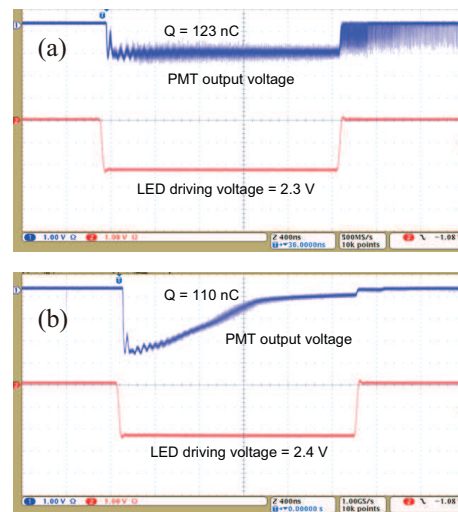


FIG. 26. Typical profile recorded by an oscilloscope during the PMT-illuminating test conducted using an LED. Rectangular voltage pulses drove the LED. Total charges  $Q$  are presented. These were estimated from the pulse current flowing from the PMT.

#### E. Coincidence

Our findings indicate that the current-readout method can be effectively applied at a high event rates featuring severe pileups. This approach seems impossible to make coincidence measurements between different detector channels, as it does not involve individual pulse identification. That is why we can avoid the pile-up effects.

However, the current-readout method can still perform coincidence (AND) operations. In the conventional pulse-counting method, the AND operation is based on two-adic (binary) logic circuits.

$$\begin{aligned} \text{TRUE} \cap \text{TRUE} &= 1 \times 1 = 1 \\ \text{TRUE} \cap \text{FALSE} &= 1 \times 0 = 0 \\ \text{FALSE} \cap \text{FALSE} &= 0 \times 0 = 0. \end{aligned} \quad (35)$$

In this case, voltage discrimination is adopted to identify whether the state has a value of one or zero.

The current-readout method, however, does not use voltage discrimination; consequently, we cannot identify the value of the state into one or zero. However, distinguishing between TRUE or FALSE is not always necessary. Notably, the output voltage  $V(t)$  represents the event flux observed at the detectors, implying that  $V(t)$  can be interpreted to be proportional to the “state.” This means that instead of viewing the problem from the perspective of two-adic Boolean algebra, we can regard  $V(t)$  as the logic signal, described either as in analog form, as a real number, or as an  $n$ -adic number. Digitization may be applied at the final stage; however, it does not have to be applied in the first stage.

Based on this, we can extend Eq.(35) from two-adic



Boolean algebra to cover operations between two real numbers as follows:

$$\begin{aligned} V_{\text{AND}}(t) &= V_1(t) \times V_2(t) \\ V_{\text{OR}}(t) &= V_1(t) + V_2(t). \end{aligned} \quad (36)$$

Eq.(36) includes Eq.(35) as a special case of  $V = 0$  or  $1$ . This extension implies a shift in our perspective from viewing TRUE or FALSE as a binary black-and-white image to considering it as a grayscale image. In this renewed framework, voltage represents TRUENESS, defined as the reliability of being regarded as TRUE.

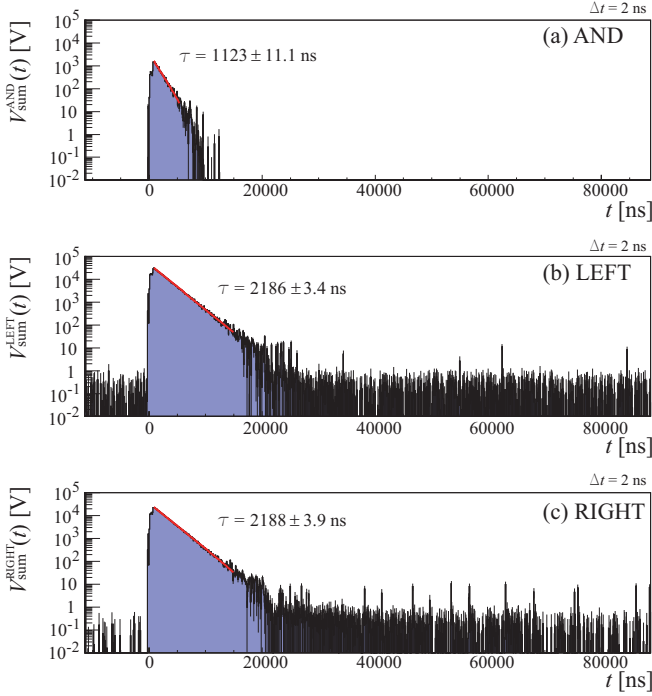


FIG. 27.  $V_{\text{sum}}(t)$  spectrum for (a) LEFT  $\times$  RIGHT, (b) LEFT, and (c) RIGHT. The spectrum shown in (a) is the sum of the spectral product  $\sum(V^{\text{LEFT}}(t) \times V^{\text{RIGHT}}(t))$  and not the product of the summed spectra  $V_{\text{sum}}^{\text{LEFT}}(t) \times V_{\text{sum}}^{\text{RIGHT}}(t)$ . Fitted results obtained using single exponential functions are shown as solid lines.

To demonstrate this idea, we attempted to coincide the spectra of two different counters. Fig.27 presents the  $V_{\text{sum}}(t)$  profiles of the (a) LEFT  $\cap$  RIGHT, (b) LEFT, and (c) RIGHT counters, using the data obtained through  $\mu\text{LV-Run0}$ . The profiles in Figs.27(b,c) are similar to the profile in Fig.12, showing a single exponential decay curve. Numerous background events are also apparent at  $t > 30,000$  ns, which are not related to muon decays and must be rejected by coinciding with the outputs of two detectors. Indeed, Kalliope has two detector layers dedicated to this purpose, but their coincidence is not requested in Figs.27(b,c).

Given that the LEFT and RIGHT counters are located opposite to the muon stopper, no real coincidence events

can simultaneously hit both the LEFT and RIGHT counters. Thus, the expected result of their coincidence must be an accidental coincidence.

Fig.27(a) presents  $V_{\text{AND}}(t)$  between the LEFT and RIGHT counters. The background signals shown in Figs.27(b,c) are no longer apparent, agreeing with the observations of conventional coincidence measurements. This result demonstrates that the current-readout method can perform coincidence measurements if the rate is not too high, revealing major pileup events.

In the high-flux region, a decay curve was observed, as shown in Fig.27(a). For this curve, the decay time constant was  $\tau_{\text{AND}} \sim \tau_{\mu}/2$ . Mathematically, this is self-explanatory because  $V_{\text{AND}}(t) = V^{\text{LEFT}}(t) \times V^{\text{RIGHT}}(t) \propto e^{-t/\tau_{\mu}} \times e^{-t/\tau_{\mu}} = e^{-t/(\tau_{\mu}/2)}$ . Nevertheless, understanding this behavior based on the probability of accidental coincidence is interesting.

Suppose there are positron events in which probability is proportional to the decay rate  $p_1 \propto e^{-t/\tau_{\mu}}$ . In this case, the accidental coincidence rate becomes proportional to event rate  $p_2$  of the other counter. The resulting coincidence rate is then proportional to  $p_1 \times p_2 \propto e^{-t/\tau_{\mu}} \times e^{-t/\tau_{\mu}} = e^{-t/(\tau_{\mu}/2)}$ . The obtained results corroborate this interpretation. We must emphasize that the result shown in Fig.27(a) does not correspond to histogram resulting from the product of two histograms,  $V_{\text{sum}}^{\text{LEFT}} \times V_{\text{sum}}^{\text{RIGHT}}$ , but rather manifests as an over-pulse summation of  $V^{\text{LEFT}}(t) \times V^{\text{RIGHT}}(t)$ . Therefore, the result does not simply demonstrate the product of two exponential functions but indicates that the voltage product can operate as a logical AND function. This implies that we can perform coincidence measurements by applying a product operation to the two  $V(t)$  time-sequence data.

Beyond radiation measurements, the application of the developed technique to logic operations could be valuable in general logic circuits. Notably, conventional two-adic Boolean algebra is suitable for strict calculations. However, to increase the data size per unit time in digital logic circuits, including computers and networks, we must increase the bus number (bus density) and/or decrease the pulse width by increasing the clock frequency.

The perspective demonstrates another possibility to increase the data size density per time and space. Beyond binary logic signals, we can extend to voltage dimensions as  $n$ -adic integers (or real numbers) to represent TRUENESS.

Circuits similar to those in Fig.28 can be constructed by replacing conventional AND (OR) gates with analog multiplying (summing) circuits. If the bus density and clock frequency reach their technical upper limits, this voltage TRUENESS idea may offer a solution.

This idea can also be applied to event tracking during radiation measurements. Instead of using black-and-white image data to fit a reconstruction curve, per usual practices (Fig.29(a)), direct grayscale image (Fig.29(b)) can be used. In that case, the image intensity represents the TRUENESS, which must be treated as the weight

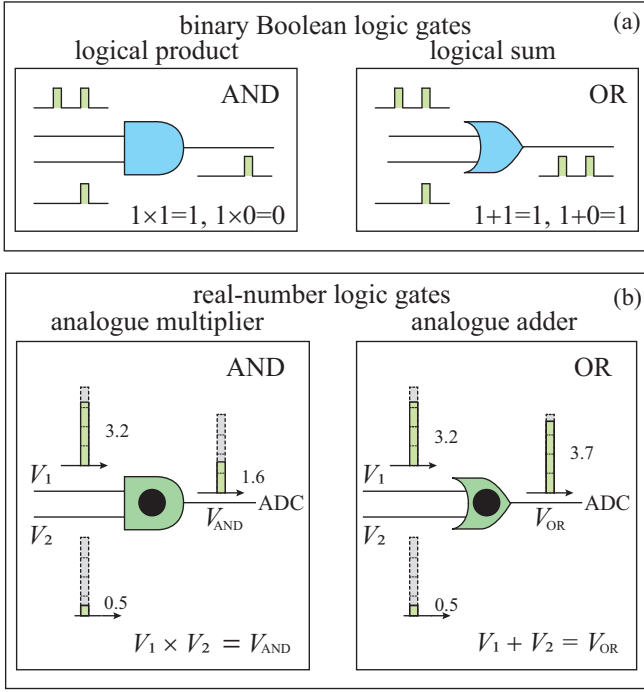


FIG. 28. AND/OR logic gates produced using analog multipliers/adders as the real-number logic gates. (a) Conventional binary logic gates. (b) Real-number logic-gates. Voltage is regarded as a representation of grayscale TRUENESS.

during fitting.

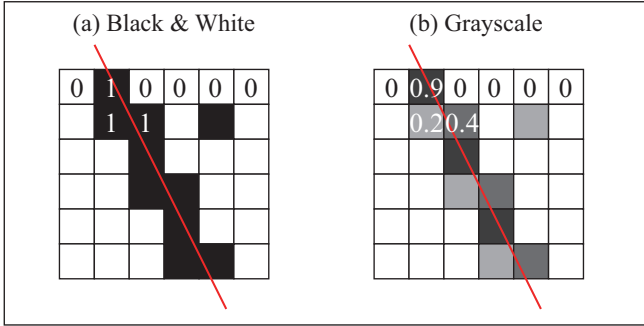


FIG. 29. Particle tracking during radiation measurements. (a) Conventional track reconstruction using hit or no-hit events, i.e., binary logic. (b) Generalized track reconstruction incorporating the reliability of the hit in each detector channel, corresponding to the voltage value (TRUENESS) shown in Fig.28.

## VII. CONCLUSION

This study developed a new current-readout technique to handle ultra-high-counting-rate measurements, suc-

cessfully confirming its application to experiments involving count rates of over 1 Gcps. We also developed an approach for random uncertainty estimation, confirming the square root property. A coincidence technique was also introduced.

## Appendix A: Beam intensity estimation

We estimated the beam intensity,  $I_{\text{beam}}$ , and Kalliope's detection efficiency,  $\epsilon$ , using the following relations.

$$\begin{aligned} n_{\text{single}} &= I_{\text{beam}} \Omega_{\text{Kalliope}} N_{\text{ch}}^{\text{single}} \epsilon_{\text{deadtime}}^{\text{single}} \epsilon \\ n_{\text{double}} &= I_{\text{beam}} \Omega_{\text{Kalliope}} N_{\text{ch}}^{\text{double}} \epsilon_{\text{deadtime}}^{\text{double}} \epsilon^2. \end{aligned} \quad (\text{A1})$$

Here,  $n_{\text{single}}$  denotes the hit rate of the total 1280 channels, and  $n_{\text{double}}$  represents the coincidence hit rate between two layers of Kalliope, which features a combined solid angle of  $\Omega_{\text{Kalliope}} = 0.16$  for 640 pairs and  $\Omega_{\text{ch}} = 2.5 \times 10^{-4}$  for a single pair.  $\epsilon$  is defined as the detection efficiency for a single channel. Furthermore,  $\epsilon_{\text{deadtime}} = n_{\text{accept}}/n_{\text{request}}$  represents a counting loss correction factor derived from the deadtime  $d$ , separately estimated for single and double counts. The values of  $d$  were obtained as detailed in Section VIC.

The total numbers of channels corresponding to single and coincidence hit events were  $N_{\text{ch}}^{\text{single}} = 1280$  and  $N_{\text{ch}}^{\text{double}} = 640$ , respectively.  $\epsilon$  was estimated by comparing  $n_{\text{single}}$  and  $n_{\text{double}}$  as  $\epsilon = n_{\text{double}}/n_{\text{single}} \times N_{\text{ch}}^{\text{single}}/N_{\text{ch}}^{\text{double}} = 0.57$ , using data corresponding to the NORMAL-intensity beam, with a minimal deadtime effect, allowing the assumption of  $\epsilon_{\text{deadtime}}^{\text{double}} \sim 1$ . This assumption was made because the decay curve recorded by Kalliope under NORMAL-intensity exposure demonstrated negligible saturation.  $\epsilon_{\text{deadtime}}^{\text{double}} \sim 0.7$  (for  $t = 0$  timing) was obtained for the data corresponding to the FULL-intensity beam.

Using Eq. (A1) with the above numbers, the  $I_{\text{beam}}$  values for the NORMAL and FULL beam were obtained.

## ACKNOWLEDGEMENTS

The  $\mu\text{LV}$  experiment at the Materials and Life Science Experimental Facility of the J-PARC was performed under the user program 2021B0324 ( $\mu\text{LV}$ -Run0) and 2022B0235 ( $\mu\text{LV}$ -Run1). We thank Naritoshi Kawamura, Shoichiro Nishimura, Soshi Takeshita, Izumi Umegaki, Takayuki Yamazaki, and Koichiro Shimomura for the detector and beamline usage. Kenji Kojima provided detailed information required to analyze the Kalliope data. Simon Zeidler, Tomoki Harada, Shunpei Iimura, Hikaru Imai, Ran Ito, Keisuke Nakamura, Hiroki Sato, Shinya Yamada, and Kazuyoshi Kurita assisted in the  $\mu\text{LV}$ -Run0, the Run1 or the H1 experiment.

## AUTHOR CONTRIBUTIONS

Maki Wakata developed the data-collection system and led the measurement at the J-PARC as her master's degree work. Lisa Hara performed the PMT tests and studied the principle as part of her undergraduate work. Shoei Akamatsu and Takuhiro Fujiie lead the

H1 measurement. Jiro Murata supervised these studies, developed the data-analysis code, performed the statistical analysis and coincidence studies, and prepared the manuscript as the corresponding author. Other authors contributed to preparing the J-PARC beam tests or checking the analysis.

- 
- [1] R. Kadono and Y. Miyake, Rep. Prog. in Physics **75**, 026302 (2012).  
 [2] T. Albahri *et al.* (Muon  $g - 2$  Collaboration), Phys. Rev. D **103**, 072002 (2021).  
 [3] R. Honda *et al.*, Prog. Theo. Exp. Phys. **2021**, 123H01 (2021).  
 [4] M. Hammad *et al.*, Applied Radiation and Isotopes **151**, 196 (2019).  
 [5] S. Ajimura *et al.*, Nucl. Instrum. Meth. A **1014**, 165742 (2021).  
 [6] J. Y. Yeom *et al.*, IEEE Trans. Nucl. Sci. **60**, 3735 (2013).  
 [7] J. Murata *et al.*, KEK Prog. Rep. **2022-7**, 89 (2023).  
 [8] J. Murata *et al.*, KEK Prog. Rep. **2023-8**, 88 (2024).  
 [9] K. M. Kojima *et al.*, J. Phys. Conf. Ser. **551**, 012063 (2014).  
 [10] N. Kawamura, JPS Conf. Proc. **33**, 011052 (2014).  
 [11] T. Yamazaki *et al.*, EPJ Web of Conf. **282**, 01016 (2023).  
 [12] Hamamatsu Photonics K.K., <https://www.hamamatsu.com/>.  
 [13] CAEN S.p.A., <https://www.caen.it/>.  
 [14] G. F. Knoll, *Radiation Detection and Measurement* (Wiley, 2010).  
 [15] LTspice, Analog Devices, Inc., <https://www.analog.com>.

